

1           **Improving thermodynamic profile retrievals from microwave**  
2           **radiometers by including Radio Acoustic Sounding System (RASS)**  
3           **observations**

4  
5  
6           Irina V. Djalalova<sup>1,2</sup>, David D. Turner<sup>3</sup>, Laura Bianco<sup>1,2</sup>,  
7           James M. Wilczak<sup>2</sup>, James Duncan<sup>1,2\*</sup>, Bianca Adler<sup>1,2</sup> and Daniel Gottas<sup>2</sup>

8  
9           <sup>1</sup> Cooperative Institute for Research in Environmental Sciences (CIRES), Boulder, CO, USA

10          <sup>2</sup> National Oceanic and Atmospheric Administration, Physical Sciences Laboratory, Boulder, CO, USA

11          <sup>3</sup> National Oceanic and Atmospheric Administration, Global Systems Laboratory, Boulder, CO USA

12          \*Now at WindESCo, Burlington, MA

13  
14  
15  
16  
17  
18  
19   Corresponding author address: Irina V. Djalalova (Irina.V.Djalalova@noaa.gov), NOAA/Physical  
20   Science Laboratory, 325 Broadway, mail stop: PSD3, Boulder, CO 80305. Tel.: 303-497-6238.  
21   Fax: 303-497-6181.

22

23 Outline

24 Abstract

25 1. Introduction

26 2. XPIA dataset

27 2.1 MWR measurements

28 2.2 Radiosonde measurements

29 ~~2.3~~ WPR-RASS measurements

30 2.4 BAO data

31 2.4 Radiosonde measurements

32 3. Physical retrievals

33 3.1 Iterative retrieval technique

34 ~~3.2 Physical retrieval bias~~ ~~3.2 Bias correction and temperature profiles of MWR~~

35 ~~observations using radiosondes or climatology~~

36 ~~3.3 Averaging kernel~~

37 ~~3.3 Analysis of physical retrieval characteristics~~

38 4. Results

39 ~~4.1 Physical retrieval statistical analysis from Akernel~~

40 ~~4.2~~ Statistical analysis of the physical retrievals up to 53 km AGL

41 ~~4.3~~ Statistics for the profiles least close to the ~~climatological profiles~~ climatology

42 4.4 Virtual temperature statistics

43 5. Conclusions

**Formatted:** Outline numbered + Level: 1 + Numbering Style: 1, 2, 3, ... + Start at: 1 + Alignment: Left + Aligned at: 0" + Indent at: 0.25"

**Formatted:** Outline numbered + Level: 1 + Numbering Style: 1, 2, 3, ... + Start at: 1 + Alignment: Left + Aligned at: 0" + Indent at: 0.25"

**Formatted:** Outline numbered + Level: 2 + Numbering Style: 1, 2, 3, ... + Start at: 1 + Alignment: Left + Aligned at: 0.25" + Indent at: 0.5"

**Formatted:** Indent: Left: 0.25", No bullets or numbering

**Formatted:** Font color: Auto

**Formatted:** Font color: Auto

**Formatted:** Outline numbered + Level: 1 + Numbering Style: 1, 2, 3, ... + Start at: 1 + Alignment: Left + Aligned at: 0" + Indent at: 0.25"

**Formatted:** Font color: Auto

**Formatted:** Font color: Auto

**Formatted:** Font color: Auto

**Formatted:** Outline numbered + Level: 1 + Numbering Style: 1, 2, 3, ... + Start at: 1 + Alignment: Left + Aligned at: 0" + Indent at: 0.25"

44 **Appendix A**

45 **Data availability**

46 **Author contribution**

47 **Acknowledgments**

48 **References**

49

50 **Abstract**

51 Thermodynamic profiles are often retrieved from the multi-wavelength brightness  
52 temperature observations made by microwave radiometers (MWRs) using regression methods  
53 (linear, quadratic approaches), artificial intelligence (neural networks), or physical-iterative  
54 methods. Regression and neural network methods are tuned to mean conditions derived from  
55 a climatological dataset of thermodynamic profiles collected nearby. In contrast, physical-  
56 iterative retrievals use a radiative transfer model starting from a climatologically reasonable  
57 ~~value~~profile of temperature and water vapor, with the model ~~run~~running iteratively until the  
58 derived brightness temperatures match those observed by the MWR within a specified  
59 uncertainty.

60 In this study, a physical-iterative approach is used to retrieve temperature and humidity  
61 profiles from data collected during XPIA (eXperimental Planetary boundary layer Instrument  
62 Assessment), a field campaign held from March to May 2015 at NOAA's Boulder Atmospheric  
63 Observatory (BAO) facility. During the campaign, several passive and active remote sensing  
64 instruments as well as in-situ platforms were deployed and evaluated to determine their  
65 suitability for the verification and validation of meteorological processes. Among the deployed

66 remote sensing instruments ~~was~~were a multi-channel MWR, as well as two radio acoustic  
67 sounding systems (RASS), associated with 915-MHz and 449-MHz wind profiling radars.

68 ~~Having the possibility to combine the information provided by the MWR and RASS~~  
69 ~~systems, in~~In this study the physical-iterative approach is tested with different observational  
70 inputs: first using data from surface sensors and the MWR in different configurations, and then  
71 including data from the RASS: into the retrieval with the MWR data. These temperature  
72 retrievals are assessed against ~~58~~ co-located radiosonde profiles. Results show that the  
73 combination of the MWR and RASS observations in the ~~physical-iterative approach~~retrieval  
74 allows for a more accurate characterization of low-level temperature inversions, and that these  
75 retrieved temperature profiles match the radiosonde observations better than the temperature  
76 profiles retrieved from only the MWR; in the layer between the surface and 53 km above  
77 ground level (AGL). Specifically, in this layer of the atmosphere, both root mean square errors  
78 and standard deviations of the difference between radiosonde and retrievals that combine  
79 MWR and RASS are improved by  $\sim 0.5^\circ\text{C}$  mostly 10-20% compared to the ~~other~~  
80 ~~methods~~configuration that does not include RASS observations. Pearson correlation  
81 coefficients are also improved.

82 ~~We provide the~~A comparison of the temperature physical retrievals to the manufacturer-  
83 provided neural network retrievals is provided in Appendix A.

84

85

86

87

88  
89  
90  
91  
92  
93  
94  
95  
96  
97  
98  
99  
100  
101  
102  
103  
104  
105  
106  
107  
108  
109

## 1. Introduction

~~To monitor~~Monitoring the state of the atmosphere for process understanding and for model verification and validation, ~~scientists rely on~~ requires observations from a variety of instruments, each one having its set of advantages and disadvantages. Using several diverse instruments allows one to monitor different aspects of the atmosphere, while combining them in an optimized synergetic approach can improve the accuracy of the information ~~we have available~~ on the state of the atmosphere.

During the eXperimental Planetary boundary layer Instrumentation Assessment (XPiA) campaign, ~~an~~ a U.S. Department of Energy sponsored experiment held at the Boulder Atmospheric Observatory (BAO) in Spring 2015, several instruments were deployed (Lundquist et al., 2017) with the goal of assessing their capability for measuring ~~flow within the~~ atmospheric boundary layer meteorological variables. XPiA investigated novel measurement approaches, and quantified uncertainties associated with these measurement methods. While

**Formatted:** Indent: First line: 0.5"

**Formatted:** Font color: Auto

**Formatted:** Outline numbered + Level: 1 + Numbering Style: 1, 2, 3, ... + Start at: 1 + Alignment: Left + Aligned at: 0" + Indent at: 0.25", Border: Top: (No border), Bottom: (No border), Left: (No border), Right: (No border), Between: (No border)

110 the main interest of the XPIA campaign was on wind and turbulence, measurements of other  
111 important atmospheric variables were also collected, including temperature and humidity.  
112 Among the deployed instruments were two identical microwave radiometers (MWRs) and two  
113 radio acoustic sounding systems (RASS), as well as radiosondes launches ~~that were used for~~  
114 ~~verification.~~

115 MWRs are passive sensors, sensitive to atmospheric temperature and humidity content  
116 that allow for a high temporal observation of the state of the atmosphere, with some  
117 advantages and limitations. In order to estimate profiles of temperature and humidity from the  
118 observed brightness temperatures (Tb), several methods could be applied such as regressions,  
119 neural network retrievals, or physical retrieval methodologies which can include  
120 ~~more~~additional information about the atmospheric state in the retrieval process. ~~Radiative~~  
121 ~~(e.g., Maahn et al. 2020). Microwave radiative transfer equations (models (e.g., Rosenkranz,~~  
122 ~~1998; Clough et al. 2005)~~ are commonly used to train statistical retrievals, or as forward models  
123 used within physical retrieval methods. Advantages of MWRs include their compact design, the  
124 relatively high temporal resolution of the measurements (2-3 minutes), the possibility to  
125 observe the vertical structure of both temperature and moisture through the ~~depth~~lower part  
126 of the troposphere during both clear and cloudy conditions, and their capability to operate in a  
127 standalone mode. Disadvantages include limited accuracy in the presence of rain because of  
128 scattering of radiation from raindrops in the atmosphere (and because water can deposit on  
129 the radome, although the instruments use a hydrophobic radome and force airflow over the  
130 surface of the radome during rain to mitigate this impact), rather coarse vertical resolution, and  
131 for retrievals the necessity to have a site-specific climatology. Other disadvantages include the

132 challenges related to performing accurate calibrations (Küchler et al., 2016, and references  
133 within), radio frequency interference (RFI), and the low accuracy on the retrieved liquid water  
134 path (LWP) especially for values of LWP less than  $20 \text{ g/m}^2 \cdot \text{m}^2$  (Turner 2007; Turner et al. 2007).

135 RASS, in comparison, are active instruments that emit a longitudinal acoustic wave  
136 upward, causing a local compression and rarefaction of the ambient air. These density  
137 variations are tracked by the Doppler radar associated with the RASS, and the speed of the  
138 propagating sound wave is measured. The speed of sound is related to the virtual temperature  
139 ( $T_v$ ) (North et al., 1973), and therefore, RASS are ~~routinely~~ used to remotely measure vertical  
140 profiles of virtual temperature in the boundary layer. Being an active instrument, the RASS is in  
141 general more accurate than a passive instrument (Bianco et al., 2017), but they also come with  
142 their ~~sets-of-own~~ disadvantages. The main limitations of RASS for ~~retrieval purposes~~ temperature  
143 measurements are ~~its~~ the low temporal resolution (typically a 5-min averaged RASS profile is  
144 measured once or twice per hour), ~~and~~ their limited altitude coverage. ~~Recent studies (, and the~~  
145 noise “pollution” that impacts local communities. Adachi and Hashiguchi (2019) have shown  
146 that ~~to make them more suitable to operate in urban areas~~ RASS could use parametric speakers  
147 to take advantage of their high directivity and very low side lobes. Nevertheless, the maximum  
148 height reached by the RASS is still limited, being a function of both radar frequency and  
149 atmospheric conditions (May and Wilczak, 1993), ~~and~~. It is determined both by the attenuation  
150 of the sound, which is a function of atmospheric temperature, humidity, and frequency of the  
151 sound source, and the advection of the propagating sound wave out of the radar’s field-of-  
152 view. Therefore, data availability is usually limited to the lowest several kilometers, depending  
153 on the frequency of the radar. In addition, wintertime coverage is usually ~~considerably~~ lower

154 than that in summer, due to ~~a higher probability~~increased attenuation of ~~stronger winds~~  
155 ~~advecting the sound wave away from the radar~~acoustic signal in ~~the winter~~cooler and drier  
156 environments.

157 To get a better picture of the state of the temperature and moisture structure of the  
158 atmosphere, it makes sense to try to combine the information obtained by both MWR and  
159 RASS. Integration of different instruments has been a topic of ongoing scientific interest ~~for~~  
160 ~~several years~~ (Han and Westwater 1995; Stankov et al. 1996; Bianco et al., 2005; Engelbart et  
161 al., 2009; Cimini et al., 2020; Turner and Löhnert, ~~2020~~2021, to name some). In this study ~~we~~  
162 particularly, the focus is on the combination of the MWR and RASS observations in the  
163 retrievals to improve the accuracy of the temperature profiles in the lowest 53 km compared to  
164 physical retrieval approaches that do not include the information from RASS measurements.  
165 Some studies have used analyses from numerical weather prediction (NWP) models as an  
166 additional constraint in these variational retrievals (e.g., Hewison 2007; Cimini et al. 2005,  
167 2011; Martinet et al. 2020); however, we have elected not to include model data in this study  
168 because we wanted to evaluate the impact of the RASS profiles on the retrievals from a purely  
169 observational perspective.

170 This paper is organized as follows: Section 2 summarizes the experimental dataset;  
171 Section 3 introduces the principles of the physical retrieval approaches used to obtain vertical  
172 profiles of the desired variables; Section 4 produces statistical analysis of the comparison  
173 between the different retrieval approaches and radiosonde measurement; finally, conclusions  
174 are presented in Section 5.

175



176 **2. XPIA ~~data~~dataset**

177 The data used in our analysis were collected during the XPIA experiment, held in Spring  
178 2015 (March-May) at ~~the~~ NOAA's ~~Boulder Atmospheric Observatory (BAO)~~ site, in Erie,  
179 Colorado (Lat.: 40.0451 N, Lon.: 105.0057 W, El.: 1584 m MSL). XPIA was the last experiment  
180 conducted at this facility, as after almost 40 years of operations the BAO 300-m tower was  
181 demolished at the end of 2016 (Wolfe and Lataitis, 2018). XPIA was designed to assess the  
182 capability of different remote sensing instruments for quantifying boundary layer structure, and  
183 was a preliminary study as many of these same instruments were later deployed, among other  
184 campaigns, for the second Wind Forecast Improvement Project WFIP2 (Shaw et al., 2019;  
185 Wilczak et al., 2019) which investigated flows in complex terrain for wind energy applications,  
186 ~~and~~ ~~where they~~ were for example used to study cold air ~~pool~~ poor pools (Adler et al., 2021) and gap  
187 flow characteristics (AdlerNeiman et al., ~~2021~~ 2019; Banta et al., 2020; ~~Neiman et al., 2019~~). The  
188 list of the deployed instruments included active and passive remote-sensing devices, and in-situ  
189 instruments mounted on the BAO tower. Data collected during XPIA are publicly available at  
190 <https://a2e.energy.gov/projects/xpia>. A detailed description of the XPIA experiment can be  
191 found in Lundquist et al. (2017), while a specific look at the accuracy of the instruments used in  
192 this study can be found in Bianco et al. (2017).

193

194 **2.1 MWR measurements**

195 Two identical MWRs (Radiometrics MP-3000A) managed by NOAA (MWR-NOAA) and by  
196 the University of Colorado (MWR-CU), were deployed next to each other at the visitor center  
197 ~600 m south of the BAO tower (see Lundquist et al., 2017 for a detailed map of the study

**Formatted:** Indent: Left: 0", Outline numbered + Level: 1 + Numbering Style: 1, 2, 3, ... + Start at: 2 + Alignment: Left + Aligned at: 0.25" + Indent at: 0.5"

**Formatted:** Indent: Left: 0.25", First line: 0"

198 area). Prior to the experiment, both MWRs were thoroughly serviced (sensor cleaning, radome  
199 replacement, etc.) and calibrated using an external liquid nitrogen target and an internal  
200 ambient target ~~and thoroughly serviced (sensor cleaning, radome replacement, etc.)~~. MWRs  
201 are passive devices which record the natural microwave emission in the water vapor and  
202 oxygen absorption bands from the atmosphere, providing measurements of the brightness  
203 temperatures. Both MWRs have 35-channels spanning a range of frequencies, with 21 channels  
204 in the lower (22-30 GHz) K-band frequency band, of which 8 channels were used during XPIA:  
205 22.234, 22.5, 23.034, 23.834, 25, 26.234, 28 and 30 GHz; and 14 channels in the higher (51-59  
206 GHz) V-band frequency band, of which all were used in XPIA: 51.248, 51.76, 52.28, 52.804,  
207 53.336, 53.848, 54.4, 54.94, 55.5, 56.02, 56.66, 57.288, 57.964 and 58.8 GHz. Frequencies in the  
208 K-band are more sensitive to water vapor and cloud liquid water, while frequencies in the V-  
209 band are sensitive to atmospheric temperature due to the absorption of atmospheric oxygen  
210 (Cadeddu et al., 2013). V-band frequencies or channels can also ~~can~~ be divided in two  
211 categories: the opaque channels, 56.66 GHz and higher, that are more informative in the layer  
212 of the atmosphere from the surface to ~1 km AGL, and the transparent channels, 51-56 GHz,  
213 that are more informative above 1 km AGL. Both MWRs observed at the zenith and at 15- and  
214 165-degree elevation angles in the north-south plane (referred to as oblique elevation scans  
215 and used as their average hereafter; note zenith views have a 90-degree elevation angle).  
216 However, when MWRs are deployed in locations with unobstructed views, oblique scans can be  
217 performed down to 5 degrees elevation angles and may provide better temperature profile  
218 accuracy in the lowest 0-1 or even 0-2 km AGL layers (Crewell and Löhnert, 2007).

219 In addition, each MWR was provided with a separate surface sensor to measure  
220 pressure, temperature, and relative humidity at the installation level that was ~2.5 m AGL.  
221 Vertical profiles of temperature (T), water vapor density (WVD), and relative humidity (RH)  
222 were retrieved in real-time during XPIA every 2-3 minutes using a neural network (NN)  
223 approach provided by the manufacturer of the radiometer, ~~Radiometrics~~ (Solheim et al. 1998a,  
224 and 1998b; Ware et al., 2003). Although the physical retrieval configurations used in this study  
225 do not exactly match the MWRNN retrieval configurations ~~used for NN retrievals~~, a comparison  
226 of both physical and neural network retrievals to the radiosonde temperature data is presented  
227 in Appendix A.

228 Both MWRs nominally operated from 9 March to 7 May 2015, although the MWR-NOAA  
229 was unavailable between 5-27 April 2015. For the overlapping dates, temperature profiles  
230 retrieved from the two MWRs showed very good agreement with less than 0.5 °C bias and  
231 0.994 correlation (Bianco et al., 2017). For this reason, and because the MWR-CU was available  
232 for a longer time period, ~~we use only the MWR-CU (hereafter simply called MWR)-) is used.~~

233 ~~▲ -----~~

234 **2.2 Radiosonde measurements**

235 ~~Between 9 March and 7 May 2015, while the MWR was operational, radiosondes were~~  
236 ~~launched by the National Center for Atmospheric Research (NCAR) assisted by several students~~  
237 ~~from the University of Colorado over three selected periods, one each in March, April, and May.~~  
238 ~~There was a total of 59 launches, mostly four times per day, around 14:00, 18:00, 22:00 and~~  
239 ~~0200 UTC (8:00, 12:00, 16:00 and 20:00 local standard time, LST). All radiosondes were Vaisala~~  
240 ~~RS92. The first 35 launches, between 9-19 March, were done from the visitor center, while the~~

Formatted: Font: Not Bold

241 11 launches, between 15–22 April, and 13 launches, between 1–4 May, were done from the  
242 water tank site, ~1000 meters apart (see Lundquist et al., 2017 for a detailed map of the study  
243 area). The radiosonde measurements included temperature, dewpoint temperature, and  
244 relative humidity, to altitudes usually higher than 10 km AGL, with measurements every few  
245 seconds.

246

### 247 **2.3 WPR-RASS measurements**

248 Two NOAA wind profiling radars (WPRs), operating at frequencies of 915-MHz and 449-  
249 MHz, were deployed at the visitor center (same location as the MWR) during XPIA. These  
250 systems are primarily designed to measure the vertical profile of the horizontal wind vector, but  
251 co-located RASS also ~~observe~~enable the observation of profiles of virtual temperature in the  
252 lower atmosphere, with different resolutions and height coverages depending on the WPR.  
253 Thus, the RASS associated with the 915-MHz WPR (hereafter referred to as RASS 915) measured  
254 virtual temperature from 120 to 1618 m with a vertical resolution of 62 m, and the 449 MHz  
255 RASS (hereafter referred to as RASS 449) sampled the boundary layer from 217 to 2001 m with  
256 a vertical resolution of 105 m. The maximum height reached by the RASS is a function of both  
257 radar frequency and atmospheric conditions (May and Wilczak, 1993), and is usually lower for  
258 RASS 915 data, as will be shown later in the analysis.

259 The RASS data were processed using a radio frequency interference (RFI)-removal  
260 algorithm (performed on the RASS spectra), a consensus algorithm (Strauch et al. 1984)  
261 performed on the moment data using a 60% consensus threshold, a Weber-Wuertz outlier  
262 removal algorithm (Weber et al., 1993) performed on the consensus averages, and a RASS

Formatted: Indent: Left: 0.25", First line: 0"

263 range-correction algorithm (Görsdorf and Lehmann, 2000) using an average relative humidity  
264 setting of 50% determined from the available observations.

265

## 266 **2.4.3 BAO data**

267 The BAO 300-m tower was built in 1977 to study the planetary boundary layer (Kaimal  
268 and Gaynor 1983). During XPIA, measurements were collected at the surface (2 m) and at six  
269 higher levels (50, 100, 150, 200, 250 and 300 m AGL). Each tower level was equipped with 2  
270 sonic anemometers on orthogonal booms, and one sensor based on a Sensiron SHT75 solid-  
271 state sensor to measure temperature and relative humidity with a time resolution of 1 s, and  
272 averaged over five minutes. The more accurate temperature and water vapor observations  
273 (Horst et al., 2016) at the BAO tower 2 m AGL level are used in the physical retrieval in place of  
274 the less accurate MWR inline surface sensor.

275 ~~The observational temperature and water vapor surface data are used from the more~~  
276 ~~accurate observations at the BAO tower 2 m AGL level (Horst et al., 2016), to replace the data~~  
277 ~~measured by the less accurate MWR inline surface sensor.~~

278

## 279 **3. Physical retrievals**

280 A

### 281 **2.4 Radiosonde measurements**

282 Between 9 March and 7 May 2015, while the MWR was operational, radiosondes were  
283 launched by the National Center for Atmospheric Research (NCAR) assisted by several students  
284 from the University of Colorado over three selected periods, one each in March, April, and May.

Formatted: Indent: Left: 0.25", First line: 0"

285 All radiosondes were Vaisala model RS92. There was a total of 59 launches, mostly four times  
286 per day, around 1400, 1800, 2200, and 0200 UTC (0800, 1200, 1600 and 2000 local standard  
287 time, LST). The first 35 launches, between 9-19 March, were done from the visitor center, while  
288 11 launches between 15-22 April, and 13 launches between 1-4 May, were done from the  
289 water tank site, ~1000 meters away from the visitor center (see Lundquist et al., 2017 for a  
290 detailed map of the study area). The radiosonde measurements included temperature, dew  
291 point temperature, and relative humidity to altitudes usually higher than 10 km AGL, with  
292 measurements every few seconds. As a first step, for additional verification, the radiosonde  
293 data from the 59 launches taken between 9 March and 4 May 2015 were compared to the BAO  
294 tower measurements, up to 300 m AGL. These observed data sets match very well, with a  
295 correlation coefficient of 0.99 and a standard deviation of ~0.7 °C. However, one radiosonde  
296 profile showed a large bias (> 5 °C) against all seven levels of BAO temperature measurements  
297 and all available Tv measurements from the RASS 915 (eight measurements up to 600 m AGL)  
298 and from the RASS 449 (nine measurements up to 1100 m AGL), therefore this particular  
299 radiosonde profile was excluded from the statistical analysis. Moreover, while accurate RASS  
300 data can be collected during rain, MWR data could be potentially deteriorated due to water  
301 deposition on the radome. Therefore, six profiles (three for March 13, and one each on May 1,  
302 3 and 4) were eliminated from the statistical evaluation. These restrictions lowered the number  
303 of total radiosonde launches used in this study to 52.

304

### 305 **3. Physical retrievals**

306 One way to combine the active and passive instruments would be to use the RASS  
307 observations up to their maximum available height, and stitch them with the profiles obtained  
308 from a physical-iterative method using MWR data. To do this, the moisture contribution to the  
309 RASS virtual temperatures could be removed by using either the relative humidity measured by  
310 the MWR or by a climatology of the moisture term. However, merging these different profiles  
311 could result in artificial jumps at the connecting heights.

312 Alternatively, a physical retrieval (PR) iterative approach can be used to retrieve vertical  
313 profiles of thermodynamic properties from the MWR and RASS observations (in a synergistic  
314 manner (e.g., Maahn et al 2020); Turner and Löhnert 2021). In this case, using a radiative  
315 transfer model, the process starts an optimal estimation-based physical retrieval is initialized  
316 with a climatologically reasonable value profile of temperature and water vapor, and is  
317 iteratively repeated until the computed brightness temperatures match those observed by the  
318 MWR within the uncertainty of the observed brightness temperatures and the RASS virtual  
319 temperatures within their uncertainties (Rodgers, 2000; Turner and Löhnert, 2014; Maahn et al.  
320 2020).

321

### 322 **3.1 Iterative retrieval technique**

323 For this study, the PR uses the TROPoe retrieval algorithm (formerly AERloe, Turner  
324 and Löhnert 2014; Turner and Blumberg 2019; Turner and Löhnert 2021). This algorithm is able  
325 to use radiance data from microwave radiometers, infrared spectrometers, and other  
326 observations as input. The microwave radiative transfer model, MonoRTM (Clough et al., 2005),

Formatted: Indent: Left: 0.25", First line: 0"

327 erves as the forward model, which is fully functional for the microwave region and was  
328 intensively evaluated previously on MWR measurements (Payne et al. 2008; 2011).

329 We start with the state vector  $\mathbf{X}_a = [\mathbf{T}, \mathbf{Q}, \text{LWP}]^T$ , where superscript T denotes transpose,  
330 and vectors and matrices are shown in bold.  $\mathbf{T}$  (K) and  $\mathbf{Q}$  ( $\text{g}/\text{kg}^{-1}$ ) are temperature and water  
331 vapor mixing ratio profiles at 55 vertical levels from the surface up to 17 km, with the distance  
332 between the levels increasing exponentially-likegeometrically with height. LWP is the liquid  
333 water path in ( $\text{g}/\text{m}^3 \text{ m}^{-2}$ ) that measures the integrated content of liquid water in the entire  
334 vertical column above the MWR, and is a scalar. For this study we have,  $\mathbf{X}_a$  with has dimensions  
335 equal to 111 x 1 (two vectors  $\mathbf{T}$  and  $\mathbf{Q}$  with 55 levels each, and LWP). We are using the The  
336 retrieval framework of Turner and Blumberg (2019), is used, but only using MWR data (no  
337 spectral infrared) and will augment. Here, we demonstrate the augmentation of the retrieval  
338 to include RASS profiles of  $\mathbf{T}_v$  and the resulting impact this has on the retrieved temperature  
339 profiles and information content.

340 The observation vector  $\mathbf{Y}$  from the beginning includes temperature and water vapor  
341 mixing ratio measured at the surface in-situ, and spectral  $\mathbf{T}_b$  measured by the MWR. The  
342 MonoRTM model  $\mathbf{F}$  is used as the forward model from the current state vector  $\mathbf{X}$ , Eq. (1), and is  
343 then compared to the observation vector  $\mathbf{Y}$ , iterating until the difference between  $\mathbf{F}(\mathbf{X})$  and  $\mathbf{Y}$  is  
344 small within a specified uncertainty- (Eq 1).

345

$$\mathbf{X}_{n+1} = \mathbf{X}_n + (\mathbf{S}_a^{-1} + \mathbf{K}^T \mathbf{S}_\epsilon^{-1} \mathbf{K})^{-1} \mathbf{K}^T \mathbf{S}_\epsilon^{-1} [\mathbf{Y} - \mathbf{F}(\mathbf{X}_n) + \mathbf{K}(\mathbf{X}_n - \mathbf{X}_a)] \quad (1)$$

347 with \_\_\_\_\_

**Formatted: Font: Bold**



$$\begin{aligned}
 \mathbf{X}_a &= \begin{bmatrix} T \\ Q \\ LWP \end{bmatrix} & \mathbf{S}_a &= \begin{bmatrix} \sigma_{TT}^2 & \sigma_{TQ}^2 & 0 \\ \sigma_{QT}^2 & \sigma_{QQ}^2 & 0 \\ 0 & 0 & \sigma_{LWP}^2 \end{bmatrix} & K_{ij} &= \frac{\partial F_i}{\partial X_j} \\
 \mathbf{S}_\varepsilon &= \begin{bmatrix} \sigma_{T_{sfc}}^2 & 0 & 0 & 0 \\ 0 & \sigma_{Q_{sfc}}^2 & 0 & 0 \\ 0 & 0 & \sigma_{Tb_{zenith}}^2 \textcircled{1} & \text{or } \sigma_{Tb_{zenith+oblique\ avrg}}^2 \textcircled{2} \\ 0 & 0 & 0 & \sigma_{Tv_{RASS915(449)}}^2 \textcircled{3\ or\ 4} \end{bmatrix}
 \end{aligned}$$

354  $\mathbf{X}_a = \begin{bmatrix} T \\ Q \\ LWP \end{bmatrix}$   $\mathbf{S}_a = \begin{bmatrix} \sigma_{TT}^2 & \sigma_{TQ}^2 & 0 \\ \sigma_{QT}^2 & \sigma_{QQ}^2 & 0 \\ 0 & 0 & \sigma_{LWP}^2 \end{bmatrix}$   $K_{ij} = \partial F_i / \partial X_j$

355 where i and j in the  $K_{ij}$  definition mark channel and vertical level, respectively, and  $\mathbf{Y}$ , depending Formatted: Font: Bold

356 on the configuration used, being equal to:

357  $\mathbf{Y}_1 = \begin{bmatrix} T_{sfc} \\ Q_{sfc} \\ T_{b_{zenith}} \end{bmatrix}$   $\mathbf{Y}_2 = \begin{bmatrix} T_{sfc} \\ Q_{sfc} \\ T_{b_{zenith+oblique\ avrg}} \end{bmatrix}$

360  $\mathbf{Y}_3 = \begin{bmatrix} T_{sfc} \\ Q_{sfc} \\ T_{b_{zenith+oblique\ avrg}} \\ Tv_{RASS915} \end{bmatrix}$   $\mathbf{Y}_4 = \begin{bmatrix} T_{sfc} \\ Q_{sfc} \\ T_{b_{zenith+oblique\ avrg}} \\ Tv_{RASS449} \end{bmatrix}$

363 The superscripts T and -1 in (1) indicate the transpose and inverse matrix, respectively. Also, Formatted: Font: Bold

364 vectors. The observation vector  $\mathbf{Y}$  and matrices the covariance matrix of the observed data,  $\mathbf{S}_\varepsilon$ , Formatted: Font: Bold

365 depending on the configuration used, are shown in bold equal to:

$$366 \quad Y_1 = \begin{bmatrix} T_{sfc} \\ Q_{sfc} \\ Tb_{zenith} \end{bmatrix} \quad S_{\varepsilon_1} = \begin{bmatrix} \sigma_{T_{sfc}}^2 & 0 & 0 \\ 0 & \sigma_{Q_{sfc}}^2 & 0 \\ 0 & 0 & \sigma_{Tb_{zenith}}^2 \end{bmatrix}$$

$$367 \quad Y_2 = \begin{bmatrix} T_{sfc} \\ Q_{sfc} \\ Tb_{zenith+oblique} \end{bmatrix} \quad S_{\varepsilon_2} = \begin{bmatrix} \sigma_{T_{sfc}}^2 & 0 & 0 \\ 0 & \sigma_{Q_{sfc}}^2 & 0 \\ 0 & 0 & \sigma_{Tb_{zenith+oblique}}^2 \end{bmatrix}$$

$$368 \quad Y_3 = \begin{bmatrix} T_{sfc} \\ Q_{sfc} \\ Tb_{zenith+oblique} \\ Tv_{RASS915} \end{bmatrix} \quad S_{\varepsilon_3} = \begin{bmatrix} \sigma_{T_{sfc}}^2 & 0 & 0 & 0 \\ 0 & \sigma_{Q_{sfc}}^2 & 0 & 0 \\ 0 & 0 & \sigma_{Tb_{zenith+oblique}}^2 & 0 \\ 0 & 0 & 0 & \sigma_{Tv_{RASS915}}^2 \end{bmatrix}$$

$$369 \quad Y_4 = \begin{bmatrix} T_{sfc} \\ Q_{sfc} \\ Tb_{zenith+oblique} \\ Tv_{RASS449} \end{bmatrix} \quad S_{\varepsilon_4} = \begin{bmatrix} \sigma_{T_{sfc}}^2 & 0 & 0 & 0 \\ 0 & \sigma_{Q_{sfc}}^2 & 0 & 0 \\ 0 & 0 & \sigma_{Tb_{zenith+oblique}}^2 & 0 \\ 0 & 0 & 0 & \sigma_{Tv_{RASS449}}^2 \end{bmatrix}$$

370 Note that ~~we are including~~ the 2-m surface-level observations of temperature and water  
 371 vapor mixing ratio ( $T_{sfc}$  and  $Q_{sfc}$ , respectively) are included as part of the observation vector  $Y$ ,  
 372 and thus the uncertainties (0.5 K for temperature and less than 0.4 g kg<sup>-1</sup> for mixing ratio) in  
 373 these observations are included in  $S_{\varepsilon}$ .

374 ~~The first guess of the state vector  $X$ ,  $X_1$  in Eq. (1), is set to be equal to the~~ The mean state  
 375 vector of the climatological estimates, or a “prior” vector  $X_a$ , which is a key component in the  
 376 optimal estimation framework and it is the first guess of the state vector  $X$ ,  $X_1$  in Eq. (1). It  
 377 provides a constraint on the ill-posed inversion problem. The prior is calculated independently  
 378 for each month of the year from climatological sounding profiles (using 10 years of data) in the

Formatted: Subscript

Formatted: Subscript

379 Denver area.  ~~$S_0$  is the~~The covariance matrix,  $S_0$ , of the “prior” vector ~~that~~ includes not only  
380 temperature or water vapor variances but also the covariances between them. Using around  
381 3,000 radiosondes launched by the NWS in Denver, ~~we interpolated~~ each radiosonde profile is  
382 interpolated to the vertical levels used in the retrieval, after which ~~we computed~~ the covariance  
383 of temperature and temperature, temperature and humidity, and humidity and humidity is  
384 computed for different levels.  ~~$K$  is the Jacobian matrix, computed using finite differences by~~  
385 ~~perturbing the elements of  $X$  and rerunning the radiative transfer model.~~

**Formatted:** Font: 11 pt, Highlight

386 ~~We start with four~~Four configurations are chosen for the observational vector  $Y$  ( $Y_1$ ,  $Y_2$ ,  
387  $Y_3$ , and  $Y_4$ ). ~~In each of these, the surface observations are obtained by the 2-m BAO in-situ~~  
388 measurements of temperature and humidity. The MWR provides  $T_b$  measurements from 22  
389 channels from the zenith scan for the zenith only configuration ( ~~$Y_1$ , which also includes the 2-m~~  
390 ~~in-situ observations of temperature and humidity~~), while when using the zenith plus oblique  $T_b$   
391 inputs ( $Y_2$ ,  $Y_3$ , and  $Y_4$ , ~~also including the 2-m in-situ observations of temperature and humidity~~)  
392 the same 22 channels were used from the zenith scans together with only the four opaque  
393 channels (56.66, 57.288, 57.964 and 58.8 GHz) from the oblique scans. Using additional  
394 measurements from the co-located radar systems with RASS, ~~we may further expand~~ the  
395 observational vector is further expanded with either RASS 915 ( $Y_3$ ) or RASS 449 ( $Y_4$ ) virtual  
396 temperature observations. The covariance matrix of the observed data,  $S_e$ , depends on the  
397 chosen  $Y_i$  as ~~it is highlighted by the red numbers~~seen in the matrix ~~description~~ $S_{e_i}$  (with  $i = 1:4$ )  
398 descriptions, with increasing dimensions from  $Y_1$  to  $Y_2$  and additional increasing dimensions to  
399  $Y_3$  or  $Y_4$  through the multi-level measurements of the RASS (Turner and Blumberg, 2019). Table

**Formatted:** Font: 14 pt

**Formatted:** Font: 14 pt, Bold

**Formatted:** Font: 14 pt

400 1 summarizes the observational information included in these four different configurations of  
 401 the PR.  
 402

	$T_{sfc}$	$Q_{sfc}$	$Tb_{zenith}$	$Tb_{oblique}$ <del>***</del>	$TV_{RASS915}$	$TV_{RASS449}$
$Y_1 = MWRz$	X	X	X			
$Y_2 = MWRzo$	X	X	X	X		
$Y_3 = MWRzo915$	X	X	X	X	X	
$Y_4 = MWRzo449$	X	X	X	X		X

403 Table 1. Four PR configurations corresponding to the four observational  $Y_i$  vectors in Eq. (1).  
 404

405 The uncertainty in the MWR  $Tb$  observations was set to the standard deviation from a  
 406 detrended time-series analysis for each channel during cloud-free periods, ~~which.~~ The method  
 407 to detect those cloud-free periods is described in detail in Section 3.2. The derived uncertainties  
 408 ranged from 0.3 K to 0.4 K in the 22 to 30 GHz channels, and 0.4 to 0.78 K in the 52 to 60 GHz  
 409 channels. We assumed that there was no correlated error between the different MWR  
 410 channels.

411 For the RASS, ~~collocated~~ co-located RASS and radiosonde profiles were compared and  
 412 the standard deviation of the differences in  $Tv$  were determined as a function of the radar's

Formatted: Space Before: 0 pt, After: 0 pt, Line spacing: Double

Formatted Table

Formatted: Space Before: 0 pt, After: 0 pt, Line spacing: Double

Formatted: Space Before: 0 pt, After: 0 pt, Line spacing: Double

Formatted: Space Before: 0 pt, After: 0 pt, Line spacing: Double

Formatted: Space Before: 0 pt, After: 0 pt, Line spacing: Double

Formatted: Space Before: 0 pt

413 signal-to-noise ratio (SNR). This relationship resulted in uncertainties that ranged from 0.8 K at  
414 high SNR values to 1.5 K at low SNR values. Again, we assumed that there was no correlated  
415 error between different RASS heights. Following ~~all~~ these assumptions, the covariance matrix  $S_e$   
416 is diagonal.

417 The Jacobian matrix,  $K$ , is computed using finite differences by perturbing the elements  
418 of  $X$  and rerunning the forward model. It has dimensions  $m \times 111$ , where  $m$  is the length of the  
419 vector  $Y_i$ , therefore its dimension increases correspondingly with the inclusion of more  
420 observational data.  $K$  makes the “connection” between the state vector and the observational  
421 data and should be calculated at every iteration.

422

### 423 ~~3.2 Physical retrieval bias~~Bias-correction and temperature profiles of MWR observations 424 using radiosondes or climatology

425 Observational errors propagate through ~~the~~ retrieval into the derived profiles (i.e. the  
426 bias of the observed data will contribute to a bias in the retrievals. ~~→~~). For that, retrieval  
427 uncertainties in Eq. (1) from  $Y = Y_1$  or  $Y_2$  derive only from uncertainties in surface and MWR  
428 data, while retrieval uncertainties from  $Y = Y_3$  or  $Y_4$  ~~are coming~~come from uncertainties in the  
429 surface, MWR, and RASS measurements.

430 ~~While the~~The bias of the retrieval depends on both the ~~sensitivity~~absolute accuracy of  
431 the forward model and ~~the~~on any observational systematic offset, ~~we can try to eliminate, or at~~  
432 ~~least to reduce, of which~~ the systematic error in the MWR observations. ~~To this aim, we could~~  
433 potentially be reduced through application of a MWR Tb bias-correction procedure. In this  
434 study, two different approaches were used for the bias-correction: the first ~~looked for clear sky~~

Formatted: Indent: Left: 0.25", First line: 0"

435 ~~analysis~~ based on a comparison to the radiosondes, while the second uses climatological profiles.  
436 The first method could be used for a field campaign where occasional co-located radiosonde  
437 launches are taken, while the second would be used for deployments without any supporting  
438 radiosonde observations.

439 For both approaches, the first step is to identify clear-sky periods during which the bias  
440 can be estimated (to reduce the degrees of freedom associated with clouds) ~~during and~~  
441 subsequently the period of bias can be removed from the measurements observed MWR Tbs.

442 One method to identify clear-sky times is to use a time-series of Tb observations in the 30 GHz  
443 liquid water sensitive channel ~~of the MWR.~~

444 The ~~random uncertainty~~ standard deviation of the MWR Tb in ~~the~~ the 30 GHz channel is  
445 calculated ~~as over a time frame of one hour centered at the radiosonde launch time.~~ The data  
446 from the zenith scan and the averaged oblique scans are reviewed separately. Liquid-cloud free  
447 periods were identified by cases where the temporal standard deviation was small (< 0.4 K),  
448 and more than 35 radiosonde profiles were classified as being launched in clear skies. The  
449 usage of the standard deviation from the time-series from the oblique scans, with the same 0.4  
450 K restriction, reduces the number of the clear-sky radiosonde profiles to 18. For those chosen  
451 18 radiosonde profiles, the Tb is calculated from radiosonde temperature profiles through  
452 MonoRTM at each of the MWR channels. The mean difference between these calculated  
453 radiosonde Tbs and measured MWR Tbs forms the Tb bias with which the MWR Tb data can be  
454 corrected. This bias-correction method will be referred to as 'radiosonde BC'.

455 While this radiosonde BC method can be employed for the XPIA dataset, for other  
456 campaigns this approach would not be possible if co-located radiosonde observations were not

457 available. For this situation, an alternative method for correcting the MWR Tb biases is  
458 presented. In this method, to choose clear-sky periods, the 30 GHz channel MWR Tb data are  
459 used on a daily basis. The standard deviation of the MWR Tb is calculated as the average of the  
460 Tb standard deviation deviations in a one-hour sliding window through all data points of a day.  
461 (It also could be computed as the standard deviation of the difference between Tb and the  
462 smoothed Tb to eliminate daily temperature variability.) Four clear-sky days have been chosen  
463 were identified using a criterion threshold of 0.34 K uncertainty in on the 30 GHz  
464 channel standard deviation: March 10 and 30, and April 13 and 29, 2015. During periods with  
465 liquid-bearing clouds overhead, this criterion is markedly higher (more than 0.7 K) and much  
466 higher for the rainy periods (> 4 K). While those calculations were applied on a daily basis, it is  
467 important to mention that the days are not uniform in terms of cloudiness or rain. Therefore,  
468 we used the data for 2-3 hours around the time of radiosonde launches to determine to which  
469 category a particular radiosonde profile belongs, clear-sky, cloudy or rain. In this way, we found  
470 that from 58 radiosonde launches used in our statistical analysis, 41 belong to the clear-sky  
471 category, 12 to cloudy but non-precipitating conditions, and 5 to rainy periods. For the four  
472 chosen clear-sky days not only were the daily uncertainties of 30 GHz Tb below 0.3 K, but both  
473 sets of uncertainties described above were extremely similar with the averaged difference less  
474 than 0.05 K.

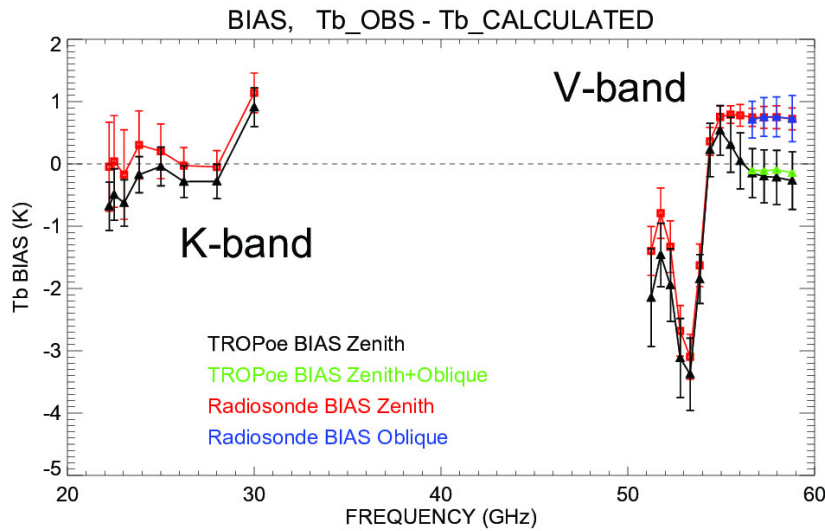
475 The Tb bias was is then computed for each of the 22 channels as the averaged difference  
476 between the observed Tb from the MWR zenith observations, and the forward model  
477 calculation applied to the prior, over these calculated Tbs at zenith using the TROPoe-retrieved  
478 profiles ( $Y_1$ ) of those selected clear-sky days, and then subsequently removed from all of the

479 This method identified spectral calibration errors in the MWR observations that could not be  
480 explained by physically realistic atmospheric profiles. This bias-correction technique will be  
481 referred to as 'TROPOe BC'.

482 Fig. 1 shows the Tb biases found for all 22 MWR channels  
483 from both bias-correction procedure only from the zenith approaches. The biases calculated  
484 with the radiosonde BC scheme are shown for all channels used in our analysis: 22 channels of  
485 the zenith scan, in red, and four V-band opaque channels of the oblique scans, in blue. The  
486 black and green triangles represent the biases calculated using the TROPOe BC approach for  
487 zenith and for zenith+oblique scans, respectively. All biases are presented with associated  
488 uncertainties (error bars representing the standard deviation over all radiosondes for



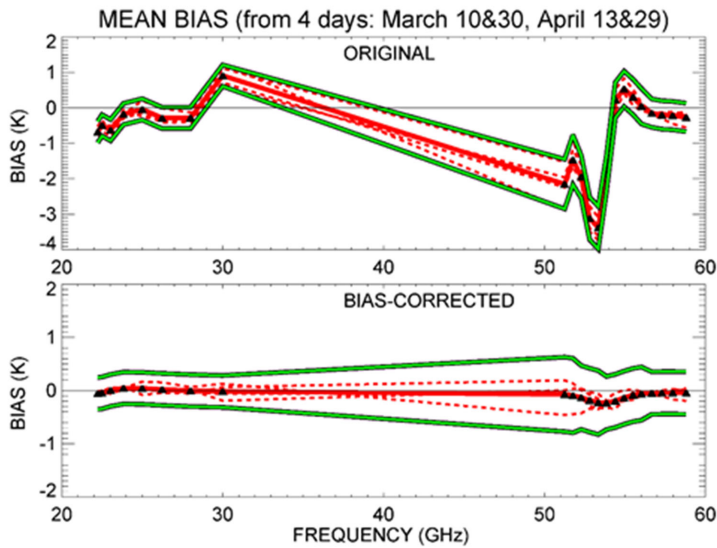
489 radiosonde BC, and mean observation Tb vector uncertainties for chosen four clear-sky days for  
 490 TROPoe BC).



491 Fig. assuming that the same 1. Tb biases derived from the radiosonde BC method (and  
 492 TROPoe BC method) in all 22 MWR channels of the zenith scan in red (and in black), and in the  
 493 four opaque channels of the oblique scans in blue (and in green).

494  
 495 The biases from the two bias-is-suitable-for-correction schemes are within the  
 496 uncertainties of each other scans. Also, we assume for most of the channels except at the higher  
 497 frequencies in the V-band. Biases in the most opaque channels are significantly affected by the  
 498 accuracy of the boundary layer temperature profiles. When TROPoe BC is used, a monthly  
 499 average prior temperature profile is used in the PR, and thus differences between this prior

500 profile and the actual temperature profile can result in a spectral bias in the more opaque MWR  
501 channels. On the contrary, the radiosonde BC uses a direct measurement of the temperature  
502 profile (from the radiosonde), and thus is more accurate. It is also important to note that, in  
503 both approaches, the biases in the opaque channels for zenith and for oblique scans (for  
504 radiosonde BC these are red and blue, respectively; and for the TROPoe BC these are black and  
505 green, respectively) are very similar to each other. This supports the assumption that the true  
506 bias is an offset that is nearly independent of the scene, soor that the sensitivity to the scene  
507 (e.g., clear or cloudy, zenith or off-zenith) is small. To investigate that, we eliminated the  
508 radiosondes launched during rainy periods (5 out of 58 cases) and found that the average  
509 temperature profiles were very little different than when all radiosonde profiles were used,  
510 with the maximum bias and RMSE absolute differences 0.12 K and 0.11 K respectively up to 5  
511 km AGL. zenith or off-zenith) is small. Fig. 1 shows the results of the bias correction for the four  
512 chosen clear sky days. The green lines on this figure indicate the MWR random errors; these are  
513 0.3-0.4 K for K-band channels and 0.4-0.7 K for V-band channels.



514  
 515 The bias-correction methods were applied by removing the corresponding calculated  
 516 biases from the MWR Tb observations before the retrievals were performed. Later in Section 4,  
 517 differences in the retrieved temperature profiles will be shown when using the two bias-  
 518 correction approaches. These differences will be more evident in the temperature profiles  
 519 exhibiting near-ground temperature inversions.

520 However, the final goal of this study is not to assess the sensitivity to different bias-  
 521 correction approaches but to verify that the inclusion of RASS observations does improve  
 522 retrieved temperature profiles, independently of the bias-correction method used.

523

524 **3.3 Analysis of physical retrieval characteristics**

525 ~~Fig. 1. Bias for the four chosen clear sky days (red dashed lines) and their mean (red solid line)~~  
526 ~~for the original observations in the top panel, and for the bias-corrected data in the bottom~~  
527 ~~panel. Green lines are the uncertainty boundaries around the mean bias. Frequencies used in the~~  
528 ~~PR algorithm are marked with black triangles in both panels.~~

530 The retrieved profiles of the four different PR configurations presented in Table 1  
531 (MWRz, MWRzo, MWRzo915, MWRzo449) were compared to the radiosonde profiles. ~~BAO~~  
532 ~~tower temperature and mixing ratio data at the seven available levels were used as an~~  
533 ~~additional validation dataset, without any interpolation.~~

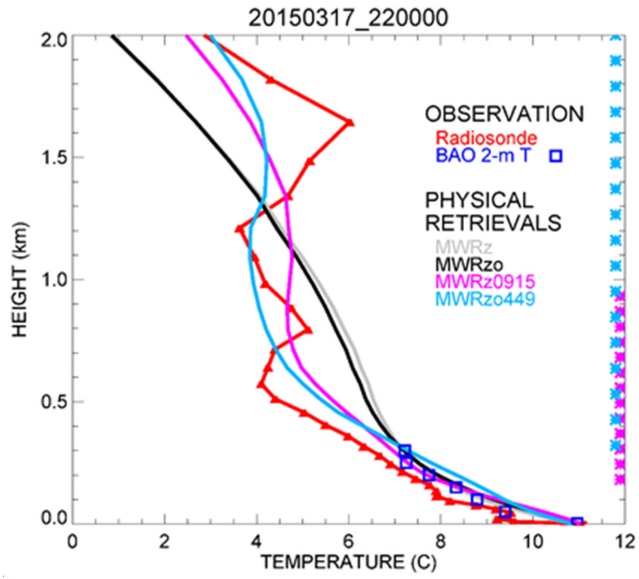
534 To compare radiosonde observations against the PR profiles, all ~~these~~ radiosonde  
535 profiles were interpolated vertically to the same PR heights, and PR profiles were averaged in  
536 the time window between 15 minutes before and 15 minutes after each radiosonde launch.  
537 Since the radiosonde ascends quite quickly in the lowest kilometers of the atmosphere (~15-20  
538 min to reach 5 km), ~~we estimated that~~ the 30-minute temporal window is estimated to be  
539 representative of the same volume of the atmosphere measured by the radiosonde. BAO tower  
540 temperature and mixing ratio data at the seven available levels were used as an additional  
541 validation dataset, without any vertical interpolation, averaged in the time window between 15  
542 minutes before and 15 minutes after each radiosonde launch.

543 ~~As an~~ As an example of the different temperature retrievals and their relative performance,  
544 data obtained on 17 March 2015 at 2200 UTC ~~is~~ are presented in Fig. 2. Temperature profiles up  
545 to 2 km AGL retrieved from the four PR configurations (MWRz, MWRzo, MWRzo915,

Formatted: Space Before: 0 pt, Border: Top: (No border),  
Bottom: (No border), Left: (No border), Right: (No border),  
Between: (No border)

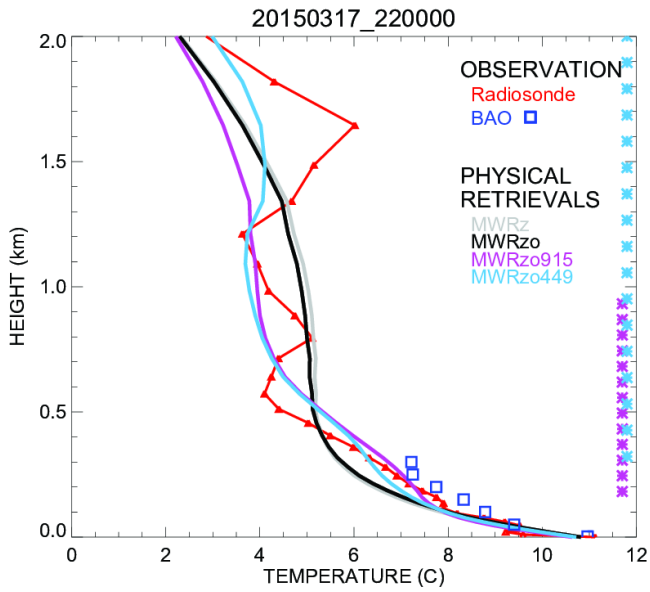
Formatted: Space Before: 0 pt

546 MWRzo449, using the radiosonde BC) are compared to the radiosonde data in red and to the  
547 BAO measurements in blue squares. Note that all four of the PRs match the BAO observations  
548 reasonably well near the ground. The MWRz and MWRzo profiles are very smooth and depart  
549 quite substantially from the radiosonde measurements, being unable to reproduce the more  
550 detailed structure of the atmospheric temperature profile measured by the radiosonde, while  
551 the MWRzo449 profile (in light-blue) demonstrates a better agreement with both the  
552 radiosonde and BAO measurements (blue squares). ~~Note that all four of the PRs match the BAO~~  
553 ~~observations reasonably well.~~ The MWRzo915 profile (in magentapurple) also tries to follow  
554 the elevated temperature inversion observed by the radiosonde, successfully only in the lower  
555 part of the atmosphere (below 1 km AGL) where RASS 915 measurements are available. This  
556 behavior will be also addressed in the following section and in the statistical analysis presented  
557 later in the manuscript.



558

559



560

561 Fig. 2. Temperature profiles obtained by the four PR configurations, after applying the  
562 radiosonde BC on the MWR Tbs: MWRz in gray, MWRzo in black, MWRzo915 in magentapurple,  
563 and MWRzo449 in light-blue. These retrievals are compared to radiosonde measurements, in  
564 red, and BAO tower observations, in blue squares. The heights with available RASS virtual  
565 temperature measurements (RASS 915 in magentapurple and RASS 449 in light-blue) are  
566 marked by the asterisks on the right Y-axis.

567

### 568 **3.3 Averaging kernel**

569 ~~The~~An asset of TROPoe is that several characteristics of the PRs can be obtained from  
570 two matrices, the averaging kernel, **Akernel**, and the posterior covariance matrix, **Sop** (Masiello  
571 et al., 2012; Turner and Löhnert, 2014) ~~from Eq. (1) can be~~, Turner and Bloomberg, 2019,  
572 calculated as:

573

$$574 \quad \mathbf{Akernel} = \mathbf{B}^{-1} \mathbf{K}^T \mathbf{S}_\varepsilon^{-1} \mathbf{K} \quad (2)$$

575 and:

$$576 \quad \mathbf{Sop} = \mathbf{B}^{-1} \quad (3)$$

577 where:

$$578 \quad \mathbf{B} = \mathbf{S}_a^{-1} + \mathbf{K}^T \mathbf{S}_\varepsilon^{-1} \mathbf{K}$$

579 ~~Both~~

580 All matrices, **Akernel**, **Sop**, and **B**, have dimensions 111 x 111 in our configuration. While  
581 the top left corner of the **Akernel** matrix (1:55, 1:55) is devoted to temperature, called further

Formatted: Space After: 0 pt

Formatted: Space After: 0 pt

Formatted: Font: Calibri, Not Bold

Formatted: Indent: First line: 0", Space After: 0 pt

Formatted: Space After: 0 pt

582 in the text **AKernel**, the next (56:110, 56:110) elements are devoted to the water vapor mixing  
583 ratio, called **AQkernel**.

584 The **AKernel** provides useful information about the calculated retrievals, such as vertical  
585 resolution and degrees of freedom for signal at each level. ~~Thus, the~~The rows of the Akernel  
586 provide the smoothing functions (Rodgers, 2000) that ~~have to~~could be applied to the retrievals  
587 (Rodgers, 2000) to help radiosonde profiles (Eq. 4) to minimize the vertical representativeness  
588 error in the comparison between the various retrievals and the radiosonde profiles due to very  
589 different vertical resolutions of these profiles. (Turner and Löhnert, 2014).

590 Using the averaging kernel, the smoothedSmoothed radiosonde observed profiles  
591 will can be therefore computed using the averaging kernel, as:

$$592 X_{smoothed\_sonde\ radiosonde} = Akernel (X_{sonde\ radiosonde} - X_a) + X_a$$

593 (3) (4)

594 The **AKernel** in Eq. (2) depends on the retrieval parameters (e.g., which datasets are  
595 used in the **Y** vector, the values assumed in the observation covariance matrix  $S_e$ , and the  
596 sensitivity of the forward model (i.e., its Jacobian), etc.), so for our four PR configurations it is  
597 possible to calculate four different kernels: **A\_MWRz, A\_MWRzo, A\_MWRzo915 and**  
598 **A\_MWRzo449**, respectively.

599 While the top left corner of the **AKernel** matrix (1:55, 1:55) is devoted to temperature,  
600 and it will be called **AT\_MWR** hereafter, the next (56:110, 56:110) elements are devoted to  
601 water vapor mixing ratio, and will be called **AQ\_MWR** from Eq. (2).

Formatted: Space After: 0 pt

Formatted: Space Before: 0 pt, After: 0 pt

Formatted: Space After: 0 pt

Formatted: Space After: 0 pt



502 For each of the four **Akernels**, a smoothed radiosonde profile can be computed for each  
503 radiosonde profile using Eq. (34). In the presence of temperature inversions or other particular  
504 structures in the atmosphere, these smoothed profiles can be quite different from each other  
505 and also from the original unsmoothed radiosonde profile.

Formatted: Font: Not Bold

506 ~~Therefore, in the statistical analysis presented later in the manuscript (in~~ Consequently,  
507 while comparison of the retrievals to the relative Akernel-smoothed radiosonde profiles can be  
508 used to minimize the vertical representativeness effects due to the different vertical resolutions  
509 of these profiles, we note that a statistical comparison between the four configurations of the  
510 observational vector would not be fair if each of their retrieved profiles is compared to a  
511 different Akernel-smoothed radiosonde profile. Therefore, in the statistical analysis presented  
512 later in the manuscript (section 4.2), mean bias, root mean square error (RMSE), and Pearson  
513 correlation coefficients will be computed between the MWR's retrievals and both the  
514 unsmoothed and smoothed radiosonde profiles, where the latter were computed using their  
515 respective Akernels. Additional observational data help to resolve the atmospheric structure in  
516 more detail, therefore we would expect to obtain better statistical evaluations from the  
517 configurations including additional RASS observations compared to the runs without RASS  
518 data, various TROPoe retrieval configurations and the unsmoothed radiosonde profiles, just  
519 interpolated to the same vertical levels of the retrieved profiles.

Formatted: Space After: 0 pt

520 The ~~improvement~~ ATkernel can help understand the differences in the retrieved  
521 temperature profiles ~~presented in Fig. 2~~ obtained by the configurations using additional RASS  
522 data ~~can be explained and clearly, shown by~~ in the ATkernel itself ~~example of Fig. 2~~. Figure 33a

Formatted: Font: Calibri, 12 pt

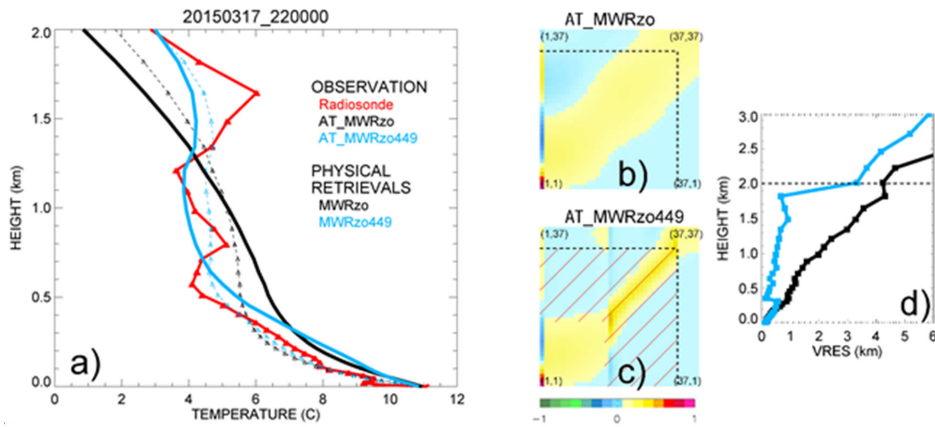
623 includes the temperature profiles of the radiosonde (unsmoothed and **ATkernel**'s smoothed)  
624 and PRs of MWRzo and MWRzo449 (panel a), and the **ATkernels** corresponding to these PRs in  
625 the color plots in the middle of the figure (panels b and c). These color plots are a schematic  
626 visualization of the 37 x 37 top left corner of the **ATkernel** matrix that illustrates the part of the  
627 **ATkernel** up to 3 km, for reference. Dash lines mark the 2 km vertical level.

628 For the same example as in Fig. 2. Due to the inclusion of RASS measurements, the  
629 **ATkernel**-smoothed radiosonde profile of the MWRzo449 configuration (dashed light-blue line)  
630 is closer to the original radiosonde data (in red) compared to the black dashed profile of the  
631 MWRzo's **ATkernel**-smoothed radiosonde profile. Additionally, the rows of the **ATkernel**  
632 provide a measure of the retrieval smoothing as a function of altitude, so the full-width half  
633 maximum (**FWHM**) of each **ATkernel** row estimates the vertical resolution of the retrieved  
634 solution at each vertical level (Maddy and Barnet, 2008; Merrelli and Turner, 2012). These  
635 plots of temperature this vertical resolution versus as a function of the height for the  
636 MWRzo PR and for the MWRzo449 PR are included in Figure 3, panel d, for the same case  
637 presented in Fig. 2. Comparison of **ATkernel** color plots and vertical resolution plots of MWRzo  
638 vs MWRzo449**3b**. This plot shows that the additional observations from the RASS 449  
639 significantly reduces the spread around the main diagonal from ~200m up to 2 km (in the layer  
640 of the atmosphere where RASS 449 measurements are available), thereby improving  
641 the vertical resolution of the retrievals (as clearly visible in panel d).

**Formatted:** Border: Top: (No border), Bottom: (No border), Left: (No border), Right: (No border), Between : (No border)

**Formatted:** Font: Not Bold

**Formatted:** Font: Not Bold



543

544

545

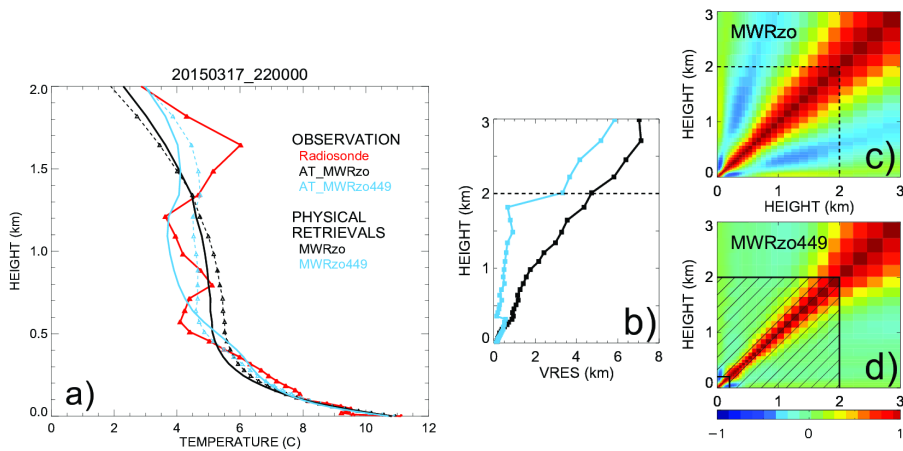
546

547

548

549

The posterior covariance matrix, **Sop**, provides a measure of the uncertainty of the retrievals while the square root of the diagonal of this matrix is used to specify the 1- $\sigma$  errors in the profiles of temperature or mixing ratio. Also, **Sop** shows the level-to-level dependency of the retrievals, and in an ideal case should have all non-diagonal elements equal to zero. Converted to a correlation matrix, it is possible to visualize these dependencies, as presented in Fig. 3c, d. The use of additional RASS data (MWRzo449 **Sop**, Fig. 3d) reduces the off-diagonal



35

650 covariances, therefore substantially decreasing the correlations in those areas compared to the  
651 MWRzo Sop (Fig. 3c).

652  
653 *Fig. 3. ~~Panel a:~~ observed temperature profiles from radiosonde, in red, from ~~AT~~ kernels*  
654 *smoothed radiosonde, ~~AT\_MWRzo~~ in dashed black, and ~~AT\_MWRzo449~~ in dashed light-blue;*  
655 *PRs from MWRzo PR in solid black, and from MWRzo449 PR in solid light-blue. ~~Middle-colored~~*  
656 *~~panels: 37x37 levels (surface to 3 km) of the Akernel matrix for temperature, b) ~~AT\_MWRzo~~ and~~*  
657 *~~c) ~~AT\_MWRzo449~~. Right panel d: vertical resolution (VRES) as a function of the height for the~~*  
658 *MWRzo PR (black), and for the MWRzo449 PR (light-blue). c) and d) 3 x 3 km (37 x 37 levels) Sop*  
659 *matrices, converted to correlation matrices, for the MWRzo PR (c), and for the MWRzo449 PR*  
660 *(d). Dashed lines on plots b)-d) mark 2 km AGL. Hatched area on panel ed marks the RASS*  
661 *measurement heights.*

**Formatted:** Font: Bold

## 662 4.2 Results

663 ~~PR profiles have been evaluated against radiosonde observations. For additional~~  
664 ~~verification, radiosonde data from 59 launches taken between 9 March and 4 May 2015 were~~  
665 ~~first of all compared to~~

666 ~~To understand the BAO tower measurements, up to 300 m AGL. These observed data~~  
667 ~~sets match very well, with a correlation coefficient of 0.99 and a standard deviation of  $\approx 0.7$  °C.~~  
668 ~~However, one radiosonde profile showed a large bias ( $> 5$  °C) against all seven levels of BAO~~  
669 ~~temperature measurements and against all PRs, therefore we decided to exclude this particular~~  
670 ~~radiosonde profile from the statistical calculations.~~

**Formatted:** Indent: First line: 0.5", Space After: 0 pt

**Formatted:** Indent: Left: 0", Outline numbered + Level: 1 + Numbering Style: 1, 2, 3, ... + Start at: 2 + Alignment: Left + Aligned at: 0.25" + Indent at: 0.5", Border: Top: (No border), Bottom: (No border), Left: (No border), Right: (No border), Between : (No border)

572

#### 573 **4.1 Physical retrieval statistical analysis from Akernel**

574 To complete the analyses on the **ATkernel** changes and dependencies from level-to-  
575 level correlations among the 4 different types of observational data used in the PRs, the  
576 **ATkernels**, averaged over all radiosonde events, are shown in Fig. 4, panels a-d, for the four PR  
577 retrieval configurations of in Table 1, in the same way as shown in **Sop** matrices were averaged  
578 over all radiosonde events, and converted to correlation matrices (Fig. 3, b-c-4). A clearly visible  
579 gradual narrowing of the spread around the main diagonal is obtained and correlation reduction  
580 in the off-diagonal elements result by the usage of the adding additional observations, from  
581 MWR zenith only (panel a Fig. 4a), to MWR zenith-oblique (panel b Fig. 4b), to the larger impact  
582 obtained by the usage of RASS 915 (panel c) and RASS 449 (panel d) data the RASS 915 (Fig. 4c),  
583 concluding with the RASS 449 (Fig. 4d) data. The mean retrieval uncertainty profile for each of  
584 the PR configurations is presented in Fig. 4e. The uncertainty of the MWRzo449 retrieval up to  
585 1 km AGL is around 0.5 °C while the other retrievals have higher uncertainties of up to 1 °C. The  
586 higher accuracy of the MWRzo449 retrievals is because that configuration has more  
587 observational information compared to the other retrieval configurations.

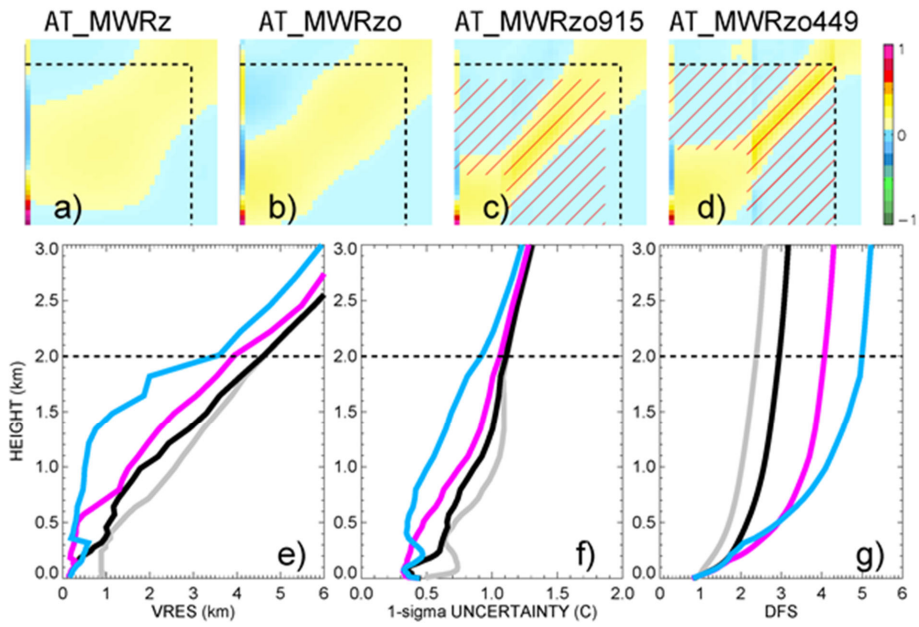
588 Other statistically important features to analyze in the PRs, besides their uncertainty,  
589 are the vertical resolution, are already introduced in the retrieval uncertainty example of Fig. 3b,  
590 and the degree of freedom for signal (DFS). These three two features are also shown in Fig. 4,  
591 panels e-g, at, derived from the Akernels of each of the heights of the retrieved solution, up to  
592 3 km AGL, and PR configuration, averaged over all radiosonde events. While the, are shown in  
593 Fig 4f and 4g. The vertical resolution (panel e Fig. 4f) shows the width of the atmosphere layer

Formatted: Highlight

Formatted: Space Before: 0 pt

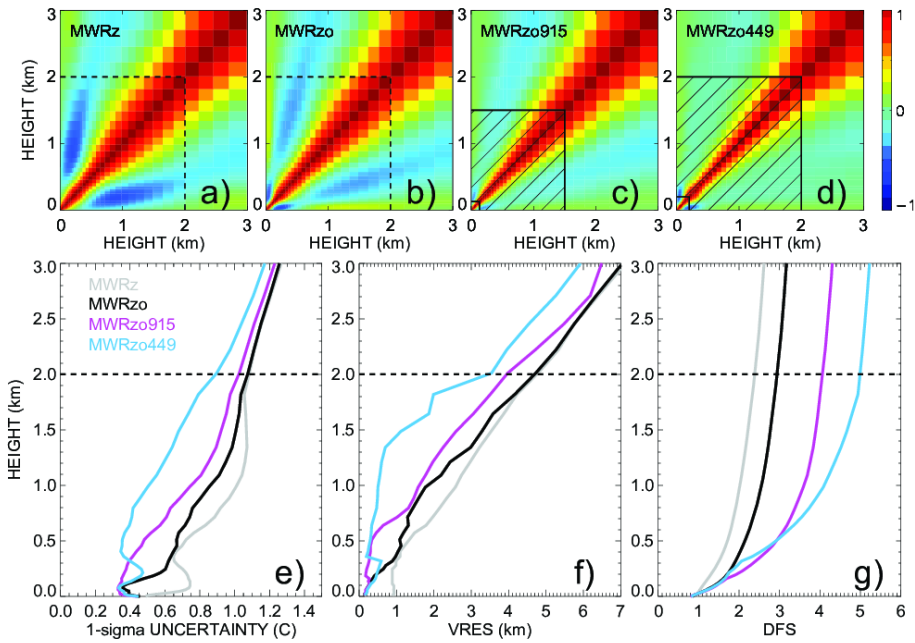
694 used for each retrieval height (~~the vertical resolution is~~, computed as the full-width half-  
695 maximum (~~FWHM; Maddy and Barnett, 2008~~) value of the averaging kernel), ~~the uncertainty~~  
696 (~~panel f~~) gives a measure of the retrieval correctness (~~computed by propagating the uncertainty~~  
697 ~~of the observations and the sensitivity of the forward model~~), and the DFS (~~panel g~~). The  
698 cumulative DFS profile (Fig. 4g) is a measure of the number of independent pieces of  
699 information ~~used~~ in the retrieved solution. observations below the specified height. For  
700 example, at the 1 km AGL level the vertical resolution of MWRzo449 ~~equals~~ is 0.5 km, ~~(i.e.~~  
701 ~~information is~~ from +/- 0.5 km around the retrieval height ~~are~~ is considered in the retrieval, ~~),~~  
702 while all other retrievals use the information from ~~+/- 2 km~~. ~~Also, the uncertainty of the~~  
703 ~~MWRzo449 retrieval up to 1 km AGL is around 0.5 °C while the other retrievals have higher~~  
704 ~~uncertainties of up to 1 °C. The higher accuracy of the MWRzo449 retrievals is because they use~~  
705 ~~more observational information compared to the other retrieval configurations~~ more than +/-  
706 1.5 km. Also, the DFS, as a cumulative measure, shows an increase in pieces of information  
707 from MWRz to MWRzo for the whole profile and from MWRzo to MWRzo915 and to  
708 MWRzo449 above ~0.2 km where RASS data are available. The DFS of MWRzo915 is higher  
709 compared to the DFS of MWRzo449 in the 0.2-0.5 km AGL layer because RASS 915 data have  
710 denser measurements there. It is also important to note that there is no additional information  
711 added to any of the retrievals above 2km AGL, i.e. the slope of the cumulative DFS profiles are  
712 equal. Despite that, the statistical analysis of the PRs up to 3 km AGL, shown in Section 4, will  
713 prove that the retrieval improvements obtained by including the RASS are found even above  
714 the height of the RASS measurements availability.

Formatted: Highlight



715

716



717

718 Fig. 4. Top four color images: AT kernels row: The mean Sops, displayed as correlation matrices,

719 for (a) MWRz (panel a), (b) MWRzo (panel b), (c) MWRzo915 (panel c), and (d) MWRzo449

720 (panel d), averaged over all radiosonde events. Hatched area on panels c) and d) marks the

721 RASS maximum measurement heights. Bottom three panels from left to right: vertical resolution

722 (VRES) in km (panel e), panels: (e) one-sigma uncertainty derived from the posterior covariance

723 matrix in °C (panel f), and, (f) vertical resolution (VRES) in km, and (g) cumulative Degree of

724 Freedom (DFS, panel g) as a function of height for temperature, averaged over all radiosonde

725 events (MWRz is in gray, MWRzo is in black, MWRzo915 is in magenta purple, and MWRzo449 is

726 in light-blue). Dashed lines mark 2 km AGL on all panels.

727



728 The improvements from MWRz (in gray) to MWRzo (in black), ~~then~~ to MWRzo915 (in  
729 ~~magenta~~purple), and finally to MWRzo449 (in light-blue) are visible in all three panels (Fig 4  
730 ~~e4e-g~~), whereas MWRzo449 has the ~~best statistical measures~~lowest 1- $\sigma$  uncertainty and  
731 highest DFS compared to the other PRs, particularly below 2 km AGL, where RASS 449  
732 measurements are available. Finally, it is interesting that below 200 m AGL the MWRzo915 has  
733 slightly ~~better statistics compared~~smaller lowest 1- $\sigma$  uncertainty and vertical resolution relative  
734 to the MWRzo449, as could be expected due to the first available height of the RASS 915 being  
735 lower (120 m AGL) than the first available height for the RASS 449 (217 m AGL) and due to the  
736 finer vertical resolution of the 915-MHz RASS. This suggests that if additional observations were  
737 available in the lowest several 100 m of the atmosphere where RASS measurements are not  
738 available, improvements might be even better closer to the surface, where temperature  
739 inversions, if present, are sometimes difficult to retrieve correctly.

**Formatted:** Space Before: 0 pt

740  
741 4. Results  
742 ~~As a matter of fact, we~~4.1 Statistical analysis of fact, we~~physical retrievals up to 3km AGL~~  
743 ~~Several cases were~~ found ~~several cases~~ during XPIA when the temperature profile  
744 ~~exhibit~~exhibited inversions, with the lowest happening in the surface layer. Figure ~~5a5~~ shows  
745 one of the most complex cases, with several temperature inversions visible in the temperature  
746 profile from the radiosonde (red line), in the temperature measurements from the BAO tower  
747 (blue squares), and in the virtual temperature measured by the RASS 449 (light blue triangles).  
748 ~~We note~~Note that the virtual temperature profile is in close agreement with the temperature  
749 measured by radiosonde. ~~Generally, the moisture contribution to the virtual temperature is less~~

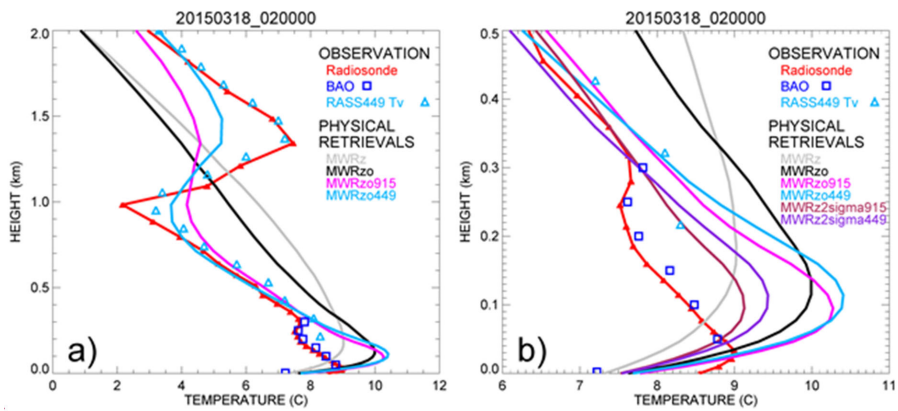
**Formatted:** Indent: First line: 0.5", Space After: 0 pt

**Formatted:** Indent: Left: 0", Outline numbered + Level: 1 + Numbering Style: 1, 2, 3, ... + Start at: 2 + Alignment: Left + Aligned at: 0.25" + Indent at: 0.5", Border: Top: (No border), Bottom: (No border), Left: (No border), Right: (No border), Between : (No border)

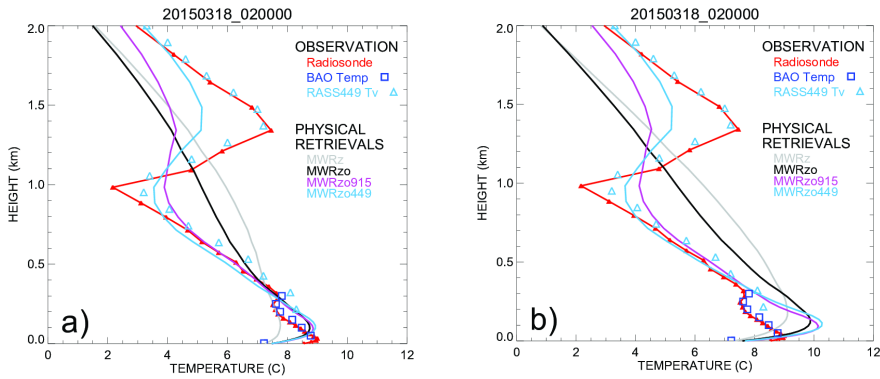
**Formatted:** Font: Bold

**Formatted:** Space Before: 0 pt

750 than a degree K, decreasing substantially for dryer air. Among the PR profiles, the PRs including  
 751 RASS data show better agreement with the radiosonde in the atmospheric layer where RASS  
 752 measurements are available, as shown in Fig. 2 for a different date. Unfortunately, this better  
 753 performance is not visible below the first available RASS measurement, i.e. from the surface up  
 754 to ~200m AGL, where the PRs with additional RASS data have the largest positive bias  
 755 compared to both radiosonde and BAO data in this layer. We found that the MWR data,  
 756 especially those from the oblique scans, in this case have a bias in the observed brightness  
 757 temperatures that propagates through the retrieval calculations, and including other  
 758 observational data is not enough to correct it in the layer between the surface data and the first  
 759 available RASS measurement.



760



761

762 Fig. 5. *Panel a, asAs* in Fig. 2 but for 18 March 2015 at 0200 UTC. The RASS 449 virtual  
 763 temperature is included as light blue triangles. *Panel b shows the same data presented in panel*  
 764 *a, but only up to 500 m AGL, and includes PR profiles in which the MWR uncertainties were*  
 765 *increased by a factor of two, MWRz915 in maroon and MWRz449 in violet*) shows the PRs  
 766 *obtained after applying the radiosonde BC, and b) shows the PRs obtained after applying the*  
 767 *TROPoe BC on the MWR Tbs.*

Formatted: Space Before: 0 pt

768

769 After several trials, we found that when RASS measurements are included, temperature  
 770 profiles in this and similar cases exhibiting inversions could be improved by increasing the  
 771 random uncertainty of MWR observations, and only using the zenith MWR measurements,  
 772 because the oblique MWR brightness temperature measurements (which give more  
 773 information in the lower layer of the atmosphere) seemingly have a bias that competes with  
 774 the active and more accurate measurements from the RASS and surface observations. In this  
 775 way, the PR approach is granted more freedom to get an optimal profile in the gap between the

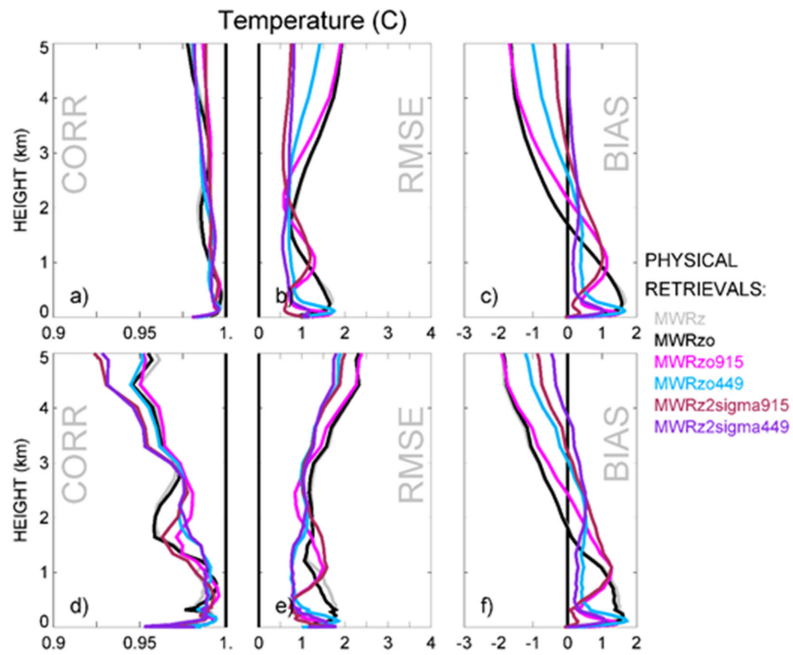
Formatted: Font: Not Italic

776 lowest RASS measurements and the surface measurement. Proof of this is presented in Figure  
777 5b, that shows the same data as in 5a, but including the profiles obtained when increasing the  
778 assumed MWR Tb uncertainties by a factor of two, hereafter called MWRz2sigma915 and  
779 MWRz2sigma449, in maroon and violet respectively. The increased accuracy of these  
780 temperature profiles compared to MWRzo915 and MWRzo449 are obvious in the layer of  
781 atmosphere closer to the surface. Later we will show that these last two PR configurations  
782 demonstrate improved statistics over all 58 cases, and also through the layer of the atmosphere  
783 up to 5 km. We note that these last two PR configurations, that were found to work well for this  
784 dataset, might not be optimal for other datasets. During XPIA the RASS measurements impact  
785 (particularly those from the RASS 449) was important in the PR approach. This might not be the  
786 case for other datasets or over different seasons, when RASS coverage might not be as good as  
787 during XPIA. For this reason, we think that attention has to be used to determine what is the  
788 best configuration to use when dealing with PR approaches. On the positive side, the advantage  
789 is that the user can determine and has control on what is the optimal configuration to use in  
790 his/her dataset, in terms of different inputs to employ and their relative uncertainty.

#### 791 **4.2 Statistical analysis of physical retrievals up to 5km AGL**

792 We calculated the relative statistical behavior of PRs for both temperature and mixing  
793 ratio, providing the comparison in two ways: first to the smoothed radiosonde using the  
794 averaging kernel matrix (as described in section 3.3), and second comparing to the original,  
795 unsmoothed, radiosonde profiles, just interpolated to the 55 PR vertical levels.

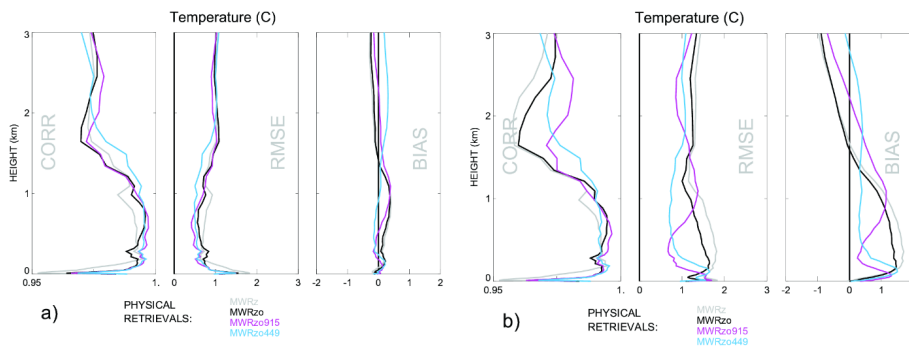
796 Figure 6 shows the statistical results of these comparisons for temperature, in terms of  
797 Pearson correlation, RMSE, and mean bias, averaged over all radiosonde events.



798  
799 Figure 5 also illustrates the difference in the temperature profiles, especially between 0-  
800 300m AGL, for the two different bias-correction schemes, which show noticeable differences in  
801 the biases of the opaque channels (especially important for the near-ground retrievals)  
802 presented in Fig. 1. As expected, the radiosonde BC method yielded a retrieved profile closer to  
803 the radiosonde temperature profile than when using TROPoe BC, for which the inversion in the

804 temperature profile close to the surface is too accentuated (particularly the black, purple, and  
805 cyan lines, all of which used oblique scan data).

806 The relative statistical behavior (Pearson correlation, RMSE, and bias) of the PRs for  
807 both temperature and mixing ratio against radiosondes is shown in Figure 6, using both bias-  
808 correction approaches. PRs obtained after applying the radiosonde BC (Fig. 6a) present overall  
809 smaller RMSE and bias (the latter almost equal to zero up to 3 km AGL) and slightly higher  
810 correlations compared to the statistics of the PRs obtained after applying the TROPoe BC (Fig.  
811 6b). This could be expected since for the comparison in Fig. 6a a subset of the radiosondes were  
812 already used for the Tb bias correction. Also, the different retrievals show a narrower  
813 distribution for the panels in Fig. 6a. Nevertheless, the results obtained when applying either



814 bias-correction methods (in Fig. 6a, b) consistently show the improvement obtained when the  
815 RASS observations are used, with relatively smaller bias and RMSE in the 3 km layer AGL. The  
816 correlation is mainly improved above 1 km, when RASS observations are included.

817 *Fig. 6. Pearson correlation, RMSE, and mean bias for temperature profiles of MWRz in gray,*  
818 *MWRzo in black, MWRzo915 in magenta, purple, and MWRzo449 in light-blue,*  
819 *MWRz2sigma915 in maroon and MWRz2sigma449 in violet, computed comparing to smoothed*

Formatted: Space After: 0 pt

820 *for the radiosonde data (using their relative **ATkernel**) in panels BC bias-correction method in a-*  
821 *e,) and against the original radiosonde measurements in panels d-f. TROPoe BC method in b).*

822 ▲ -----\*  
823       These results confirm the superiority of the MWRz2sigma449 temperature retrieval  
824 over the other PRs. While this is not true at all heights, this retrieval shows improved  
825 distribution of RMSE and bias for the atmospheric layer up to 5 km AGL. The differences  
826 between the MWRz2sigma915 and the MWRzo915 profiles are similar to those between the  
827 MWRz2sigma449 and the MWRzo449 profiles, reducing the drastic bias found in the layer  
828 closer to the ground. The differences between the two ways of comparison, against the  
829 smoothed **ATkernel** or the original radiosonde data, are small in terms of RMSE and bias, but  
830 more evident in terms of correlation as can be expected because of the smoothing technique  
831 applied to the radiosonde profiles through Eq. (3). Above and below ~1.6 km AGL the bias,  
832 RMSE, and correlation profiles of the PRs show very different behavior. While statistical scores  
833 above ~1.6 km AGL are very similar for the four PRs introduced in Table 1, they are better for  
834 the MWRz2sigma915 and MWRz2sigma449 PRs, especially when compared to the smoothed  
835 radiosonde profiles. Differences between the profiles show more variability in the lowest ~1.6  
836 km where most of the active RASS measurements are available. Also, while both PR profiles  
837 related to the RASS 449, MWRzo449 and MWRz2sigma449, have almost constant bias and  
838 RMSE from 200m up to at least 3 km, the RASS 915-based PR profiles, MWRzo915 and  
839 MWRz2sigma915, have biases and RMSEs that vary with height. Due to the lower first range  
840 gate of the RASS 915 measurements, the PR profile of MWRz2sigma915 has the smallest bias  
841 and RMSE compared to all other PR profiles in the surface to 200 m layer. With quickly

**Formatted:** Font: Not Bold, Italic

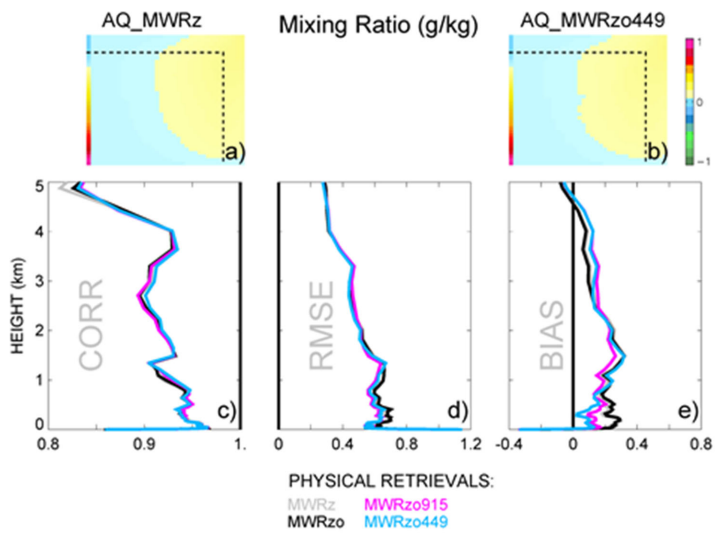
**Formatted:** Indent: First line: 0"

842 decreasing availability of RASS 915 measurement above this layer, the bias and RMSE of  
843  $MWRz_{0.915}$  and  $MWRz_{2\sigma_{915}}$  became larger, and in some higher layers even larger than  
844 the corresponding statistical measures of  $MWRz$  and  $MWRz_0$ . This marks the importance of  
845 active measurements spanning a prominent vertical layer to provide a useful application of  
846 these data in a radiative transfer model.

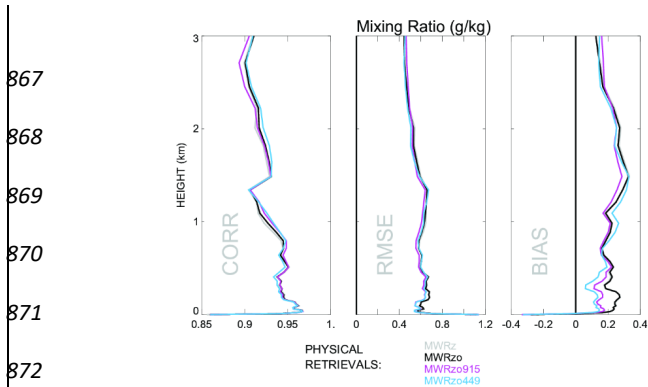
847 Besides temperature profiles, the ~~PR retrievals~~ PRs also provide water vapor mixing ratio  
848 profiles. It is understandable that the different configurations of PRs are not noticeably  
849 different from each other in relation to moisture, because the  $T_v$  observations from the RASS  
850 are dominated by the ambient temperature (not moisture), and thus have little impact on the  
851 water vapor retrievals. ~~Figure 7 includes the two AQ kernels corresponding to the PRs  $MWRz$   
852 and  $MWRz_{0.449}$  in panels a and b, which~~ We found that the AQ kernels are averaged over all  
853 ~~radiosonde events and appear to be~~ almost identical. ~~More detailed~~ for all four PR  
854 configurations (not shown). Detailed statistical ~~estimation~~ evaluation of the PRs mixing ratio  
855 profiles are presented in Fig. 7 ~~c-e~~, also averaged ~~throughover~~ all radiosonde events, and show  
856 very similar correlations, RMSEs, and biases for all PRs ~~included in the figure, meaning, implying~~  
857 that the impact of including RASS observations in the retrieval is minimal on this variable.  
858 Finally, it is noted that Fig. 7 shows the mixing ratio of the data from TROPoe BC. The  
859 radiosonde BC mixing ratio results are almost identical.

Formatted: Space After: 0 pt





860  
 861 *Fig. 7. Top two color images: AQ kernels for MWRz (panel a) and MWRzo449 (panel b),*  
 862 *averaged over all radiosonde events and shown up to 3 km AGL with dash lines mark 2 km AGL*  
 863 *on both panels. Bottom three panels are the same as panels d-f in Figure 6, but for mixing ratio*  
 864 *estimation.*



867  
868  
869  
870  
871  
872  
873 *Fig. 7. Same as the panels in Fig. 6b, but for mixing ratio, when using the TROPoe BC method on*  
874 *the MWR Tbs.*

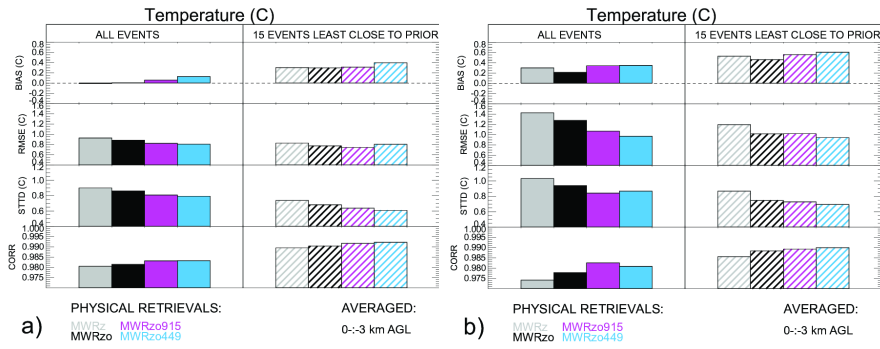
876 **4.32 Statistics for cases far from the climatological mean**  
877 **the profiles least close to the**  
878 **climatology**

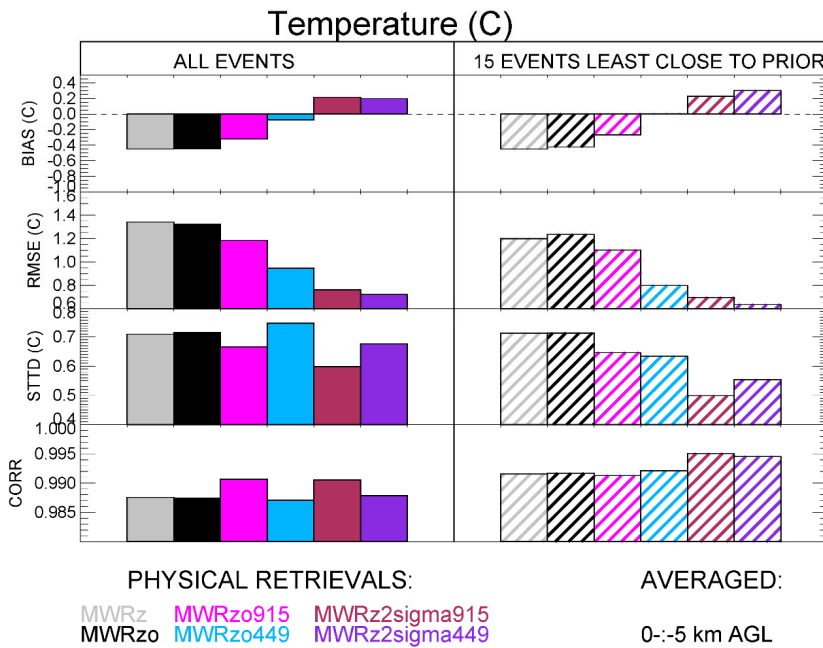
879 Physical retrievals use climatological data as a constraint ~~or for building the statistical~~  
880 ~~relationships used~~ in the retrieval. Statistically, the averaged profiles of both temperature and  
881 moisture variables are very close to the climatological averages. However, the most interesting  
882 and difficult profiles to retrieve are the cases furthest from ~~the~~ climatology (Löhnert and Maier,  
883 2012). To check the behavior of the retrieved data in such ~~events, we~~ “extreme” cases, the  
884 ~~RMSE was~~ first calculated ~~the RMSE~~ for each radiosonde profile relative to the prior profiles for  
885 ~~4237~~ vertical levels from the surface up to ~~53~~ km AGL, and then ~~we selected~~ the 15 cases with  
886 the largest 0-~~5~~km~~3~~ km layer averaged RMSEs compared to the prior. ~~All comparisons are done~~  
~~against the corresponded smoothed ATkernel radiosonde data, using AT\_MWRz, AT\_MWRzo,~~

Formatted: Indent: Left: 0.25", First line: 0"

887 **AT\_MWRzo915, AT\_MWRzo449, AT\_MWRz2sigma915, AT\_MWRz2sigma449** for all six PRs.  
 888 were selected.

*Formatted: Font: Italic*





889  
 890  
 891 Fig. 8. From top to bottom: biases (retrievals minus *ATkernel*-radiosonde), RMSEs, standard  
 892 deviations of the difference between retrievals and *ATkernel*-radiosonde, and Pearson  
 893 correlations for the *sixfour* PR configurations *so far introduced*, averaged from the surface to *53*  
 894 km AGL, *averaged and* over all radiosonde data (solid boxes), and *averaged* over the 15 *events*  
 895 *furthest from the prior extreme cases* (hatched boxes). *The data in panels a) use radiosonde BC,*  
 896 *and in b) TROPoe BC on the MWR Tbs.*

897  
 898 Figure 8 shows the temperature statistical analysis for the entire radiosonde data set  
 899 (solid boxes) and *to just for* the fifteen *chosen*-events *far from the climatological mean* (hatched

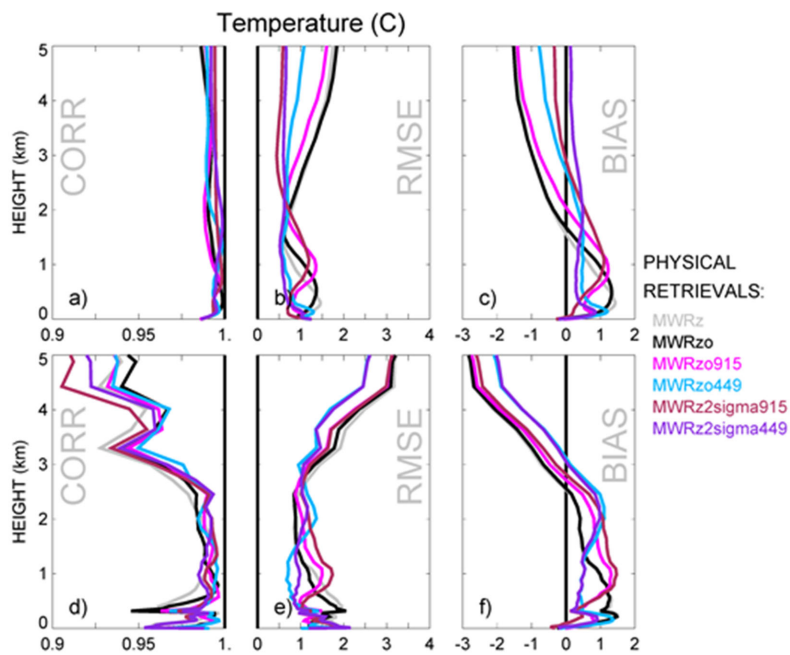
900 boxes) for bias, RMSE, standard deviation of ~~retrieval~~the differences ~~to the~~between retrievals  
901 and radiosonde data, and Pearson correlation, calculated as the weighted averaged over the  
902 ~~4237~~ vertical heights up to ~~53~~ km AGL. ~~The vertical resolution of the Physical Retrievals is not~~  
903 ~~uniform, with more frequent levels closer to the surface. If a simple average of the data from all~~  
904 ~~levels is used, the near-surface layer will be weighted more compared to the upper levels of the~~  
905 ~~retrievals. To avoid this, a vertical average over the lowest 5km AGL is performed using weights~~  
906 ~~at each vertical level determined by the distance between the levels.~~<sup>1</sup>

907 Differences in the statistics when using the entire radiosonde data set or the fifteen  
908 ~~extreme~~ profiles ~~furthest from the prior~~ are noticeable, ~~especially for bias and RMSE, but also~~  
909 ~~for the standard deviation. All~~ statistical estimators. The PRs that include RASS observations  
910 show better performance compared to the strictly MWR-only PR profiles (i.e., MWRz and  
911 MWRzo) for almost all statistical comparisons. ~~Also, the statistical behavior of the~~  
912 ~~MWRz2sigma915 and MWRz2sigma449 retrievals are the best in terms of RMSE and standard~~  
913 ~~deviation~~ This improvement is larger for all events and for RMSE, standard deviation, and  
914 correlation coefficient, for the fifteen profiles furthest from the climatological average. Fig. 8  
915 also shows that RMSE, standard deviation and correlation have improved scores for the 15  
916 events furthest from the prior when compared to all temperature profiles for all the PRs using  
917 active RASS measurements. the TROPoe BC (Fig. 8b) compared to the PRs using the radiosonde  
918 BC (Fig. 8a). Three statistical estimators, RMSE, standard deviation, and Pearson correlation

---

<sup>1</sup> The vertical grid used in the PRs is not uniform, with more frequent levels closer to the surface. If a simple average of the data from all levels is used, the near-surface layer will be weighted more compared to the upper levels of the retrievals. To avoid this, a vertical average over the lowest 3 km AGL is performed using weights at each vertical level determined by the distance between the levels.

919 show overall better values for the 15 extreme cases compared to the whole radiosonde  
920 dataset, for all PR configurations and both BC approaches. This is due to the fact that for this  
921 dataset the monthly averaged radiosonde profiles (for March and May particularly) depart  
922 quite substantially from the monthly prior profiles. For example, the averaged radiosonde  
923 profile in March is warmer by ~7 °C compared to the March prior (and in May by ~5 °C) in the  
924 first 3 km AGL. Consequently, the extreme cases (mostly found in March) have the warmest  
925 radiosonde temperature profiles, but are overall closer to the monthly averaged radiosonde  
926 profiles.



927

928 Fig. 9. The Table 2 includes the same data as Fig. 6 in Figure 8 but for the temperature  
 929 over 15 furthest from prior radiosonde profiles.

Formatted: Font: Not Italic  
 Formatted: Font: Not Italic  
 Formatted: Font: Not Italic

930  
 931 To investigate the vertical structure as a percentage of the error statistics for the 15  
 932 events furthest from the radiosonde climatology, profiles of correlation, RMSE and bias for  
 933 these events are shown in Figure 9 for the layer 0-5 km. The MWRz2sigma915 and  
 934 MWRz2sigma449 profiles, having the best averaged statistics in Fig. 8, are seen as good as, or  
 935 better, than the other methods for the 0-2 km layer. Importantly, for heights above 2km AGL,  
 936 where there is no additional observational data from RASS, all of the PRs with RASS are closer  
 937 to the "true" radiosonde temperature compared to the PRs without RASS.

938  
 939 **4.4 Virtual temperature statistics**

940 The above analysis confirms the superiority of MWRz2sigma915 and  
 941 MWRz2sigma449 improvement, compared to the other PRs for MWRz retrievals.

942  
 943  
 944  
 945  
 946  
 947

<u>0-3 km AGL</u>	<u>ALL EVENTS</u>		<u>15 EVENTS LEAST CLOSE TO THE PRIOR</u>
-----------------------	-------------------	--	---

<u>RADIOSONDE BIAS-CORRECTION</u>									
	<u>MWRz</u>	<u>MWRzo</u>	<u>MWRzo</u> <u>RASS915</u>	<u>MWRzo</u> <u>RASS449</u>		<u>MWRz</u>	<u>MWRzo</u>	<u>MWRzo</u> <u>RASS915</u>	<u>MWRzo</u> <u>RASS449</u>
<u>RMSE</u>	<u>0%</u>	<u>5%</u>	<u>11%</u>	<u>13%</u>		<u>0%</u>	<u>7%</u>	<u>10%</u>	<u>3%</u>
<u>STTD</u>	<u>0%</u>	<u>4%</u>	<u>10%</u>	<u>12%</u>		<u>0%</u>	<u>8%</u>	<u>14%</u>	<u>17%</u>
<u>CORR</u>	<u>0%</u>	<u>0.1%</u>	<u>0.3%</u>	<u>0.3%</u>		<u>0%</u>	<u>0.1%</u>	<u>0.2%</u>	<u>0.3%</u>
<u>TROPoe BIAS-CORRECTION</u>									
<u>RMSE</u>	<u>0%</u>	<u>10%</u>	<u>25%</u>	<u>32%</u>		<u>0%</u>	<u>15%</u>	<u>15%</u>	<u>21%</u>
<u>STTD</u>	<u>0%</u>	<u>9%</u>	<u>18%</u>	<u>16%</u>		<u>0%</u>	<u>14%</u>	<u>16%</u>	<u>20%</u>
<u>CORR</u>	<u>0%</u>	<u>0.4%</u>	<u>0.9%</u>	<u>0.7%</u>		<u>0%</u>	<u>0.3%</u>	<u>0.4%</u>	<u>0.4%</u>

948

949 Table 2. Retrieval improvements for different RASS/MWR configurations as a percentage  
 950 compared to MWRz.

951

952 The results presented in Table 2 show improvements in all statistical estimations when  
 953 including RASS observations, with improvements in RMSE between 10 and 20 %, demonstrating  
 954 the positive impact derived by the inclusion of the active measurements, regardless of the bias-  
 955 correction method used, but larger for the TROPoe BC data because there is more room for  
 956 improvement when this dataset BC method is used. Improvements in the Pearson correlation  
 957 coefficients are small because correlation, determined during XPIA by the overall temperature  
 958 structure with height and diurnal cycle, is already good, leaving little room for improvement.

959



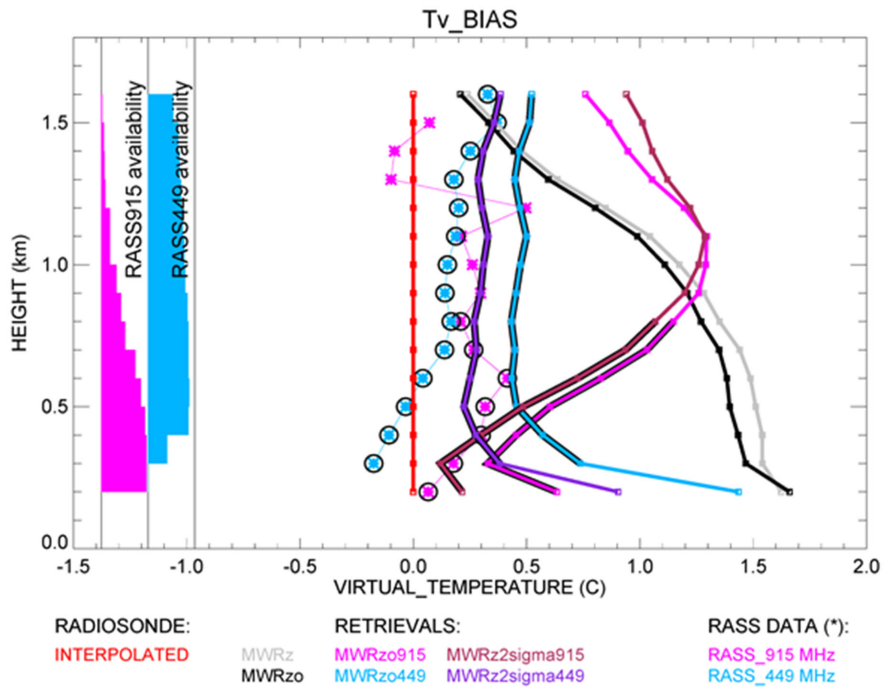
960 **4.3 Virtual temperature profile statistics**

961 Using the physical retrieval outputs, “retrieved virtual temperature profiles” can also be  
962 calculated. In this section ~~we show~~ the direct comparison of ~~the retrieved profiles to the~~  
963 ~~original radiosonde and RASS virtual temperature profiles. Using temperature and moisture~~  
964 ~~retrieval output, we calculated “these retrieved virtual temperature profiles” and interpolated~~  
965 ~~all profiles and RASS data on a regular vertical grid, going from 200 m to 1.6 km with 100 m~~  
966 ~~range, for easy~~ and RASS virtual temperature profiles to the original radiosonde is shown. With  
967 this comparison, we want to show how the biases of the retrieved profiles relate to the original  
968 RASS Tv biases.

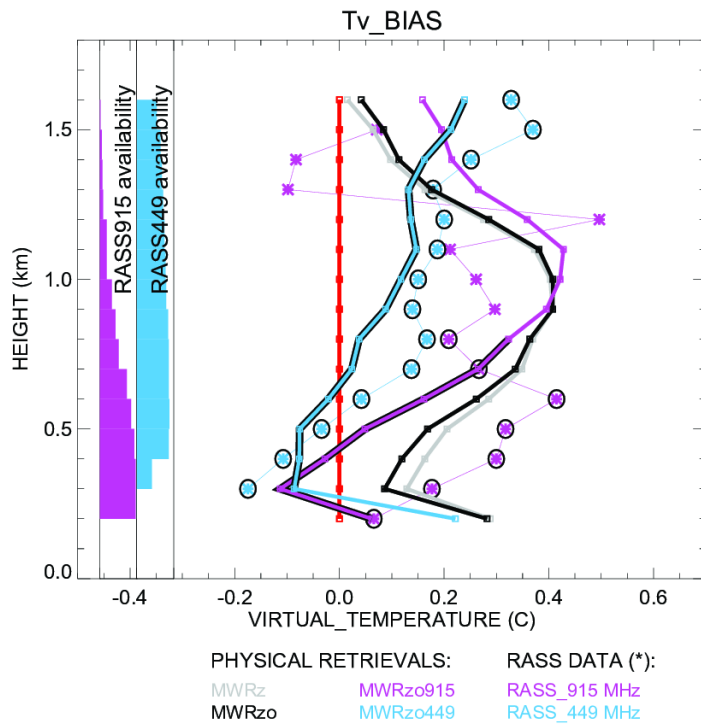
969 Figure ~~109~~ shows Tv retrieved profile biases compared to the original radiosonde data  
970 as solid lines, and RASS 915 and RASS 449 Tv bias as asterisks. RASS data are interpolated on a  
971 regular vertical grid, going from 200 m to 1.6 km with a 100 m range, for easy comparison.

972 A zero bias is denoted by the red line. On the left side of the figure ~~we show the~~ bar  
973 charts of the RASS measurement availability are shown as a function of height. The widest part  
974 of these charts corresponds to 100% data availability. Heights with RASS availability greater  
975 than 50% are marked with additional circles over the asterisks.

Formatted: Space After: 0 pt



976



977

978 *Fig. 109. Bias of virtual temperature for all ~~six~~ PR configurations compared to the original*

979 *radiosonde measurements. RASS data are marked by asterisks and by additional circles for the*

980 *RASS data with more than 50% availability, according to the availability bar charts on the left.*

981 *All PRs profiles are derived after applying the radiosonde BC method.*

982

983 While RASS 449 data are available at almost all heights up to 1.6 km, the RASS 915 data

984 availability decreases considerably with height, lowering to 50% availability around 800 m AGL.

985 ~~All~~ The PRs with input from that include RASS data, MWRzo915 and MWRzo449, ~~and~~

Formatted: Space After: 0 pt

986 ~~MWRz2sigma915 and MWRz2sigma449~~, are also marked with additional black lines at the  
987 heights with at least 50% of relative RASS data availability. ~~This~~In agreement with Fig. 6a, this  
988 figure clearly shows the superiority of ~~MWRz2sigma449 the MWRzo449 and MWRz2sigma915~~  
989 ~~MWRzo915~~ (in the layer with > 50% RASS ~~915~~-data availability) compared to the MWRz and  
990 MWRzo configurations, which do not include RASS data, ~~as well as to MWRzo915 and~~  
991 ~~MWRzo449 which include RASS data and MWR zenith and oblique data.~~ For MWRzo449 and  
992 ~~MWRz2sigma449 profiles~~, RASS 449 data were almost always available, therefore it is easy to  
993 identify ~~similar features~~a similarity between the Tv bias profiles of the RASS 449 and the PRs  
994 including it. Thus, for the MWRzo449 ~~and MWRz2sigma449~~ the Tv bias is more uniform through  
995 the heights compared to all other PRs that do not include RASS data. Moreover, ~~because it is~~  
996 noted a roughly constant offset between the MWRzo449 Tv and ~~MWRz2sigma449~~RASS 449 Tv  
997 ~~bias~~profiles follow tightly the trend of the RASS 449 ~~with height, the their averaged~~  
998 ~~difference between MWRzo449~~equal to ~0.08 °C (when the radiosonde BC is used), and ~~RASS~~  
999 ~~449 biases equals to~~ ~0.32 °C and the difference between MWRz2sigma449 and RASS 449  
1000 ~~biases equals~~ ~0.14 °C (when the TROPoe BC is used, not shown), over the ~1.3 km (0.3-1.6 km)  
1001 atmospheric layer where ~~most~~more than 50% of the RASS 449 measurements are available,  
1002 uniformly distributed through the heights. ~~Finally, the average differences between these~~  
1003 ~~MWRzo449 and MWRz2sigma449 Tv profiles and the radiosonde virtual temperature equal~~  
1004 ~0.56 °C and ~0.34 °C respectively. We note that as an alternative to using the PR temperature  
1005 ~~profiles at all heights, one could consider replacing the PR temperatures with RASS~~  
1006 ~~observations up to~~The inclusion of the RASS into the PRs does reduce the values of the biases  
1007 in the maximum height reached by retrievals even below the RASS, and then use values of the PR

1008 retrieval above that. To do this the moisture contribution to the RASS virtual temperatures  
1009 could be removed by using either the relative humidity measured by radiometer or by a  
1010 climatology of the moisture term RASS biases.

1011

## 1012 5. Conclusions

1013 In this study ~~we used the~~ data collected during the XPIA field campaign were used to  
1014 test different configurations of a physical-iterative retrieval (PR) approach in the determination  
1015 of temperature and humidity profiles from data collected by microwave radiometers, surface  
1016 sensors, and RASS measurements. ~~We tested the~~ The accuracy of several PR configurations, ~~was~~  
1017 tested: two ~~that~~ configurations made use only of surface observations and MWR observed  
1018 brightness temperature (zenith only, MWRz<sub>z</sub>; and zenith plus oblique, MWRz<sub>o</sub>), ~~and~~; while two  
1019 others ~~that~~ included the active virtual temperature profile observations available from ~~two~~ co-  
1020 located RASS (one, RASS 915, associated with a 915-MHz<sub>z</sub>; and the other, RASS 449, associated  
1021 with a 449-MHz wind profiling radar). Radiosonde launches were used for verification of the  
1022 retrieved profiles. In Appendix A, the performance of MWRz and MWRz<sub>o</sub> retrieved profiles and  
1023 Neural Network retrieved profiles were also used for comparison (see Appendix A) against the  
1024 radiosondes was evaluated.

1025 ~~Inclusion~~ To remove any observational systematic error in the MWR Tb observations,  
1026 two bias-correction procedures were tested. The first one takes advantage of the many  
1027 radiosondes launched during XPIA, and the second one uses climatological profiles. As  
1028 expected, the radiosonde bias-correction method gives retrieved profiles closer to the  
1029 radiosonde temperature profiles than when using the climatological based method.

**Formatted:** Indent: Left: 0", Outline numbered + Level: 1  
+ Numbering Style: 1, 2, 3, ... + Start at: 2 + Alignment:  
Left + Aligned at: 0.25" + Indent at: 0.5"

**Formatted:** Line spacing: Double

**Formatted:** Line spacing: Double, Border: Top: (No  
border), Bottom: (No border), Left: (No border), Right: (No  
border), Between : (No border)

1030 Nevertheless, our results show that regardless of the bias-correction method used, the  
1031 inclusion of the observations from the active RASS instruments in the PR approach improves  
1032 the accuracy of the temperature profiles, ~~particularly when~~ by around 10-20% compared to the  
1033 PR configuration using only surface observations and MWR observed brightness temperature  
1034 inversions are present from the zenith scan. Of the PRs configurations tested, ~~we find~~ generally  
1035 better statistical agreement is found with the radiosonde observations when the RASS 449 is  
1036 used together with the surface observations and brightness temperature from ~~only the zenith~~  
1037 ~~MWR observations and doubling the random radiometric uncertainty on the MWR observations~~  
1038 ~~(MWRz2sigma449) relative to the uncertainty calculated over the selected clear sky days. This~~  
1039 ~~configuration is also more accurate compared to MWRz0915 or MWRz2sigma915 (which use~~  
1040 ~~RASS 915 observation), because of the deeper RASS 449 height coverage. The larger assumed~~  
1041 ~~radiometric uncertainty in the MWR Tb observations allows the retrieval to overcome both (a)~~  
1042 ~~the small systematic errors that exist between the MWR observed Tb values and the RASS~~  
1043 ~~measurements and (b) the systematic errors that exist in forward microwave radiative models~~  
1044 ~~(Cimini et al. 2018), the zenith and averaged oblique MWR observations.~~

1045 ~~We also selected~~ The AKernel and the posterior covariance matrices for temperature are  
1046 used to derive the one-sigma uncertainty, vertical resolution, and cumulative degree of  
1047 freedom as a function of height for the different PRs, and the level-to-level correlated  
1048 uncertainty of the retrievals. Results show that the inclusion of the active instruments improves  
1049 all of the above-mentioned variables in the 0-3km layer, including at heights between 2-3km  
1050 that are above the maximum RASS height. Thus, the positive impact of the RASS observations  
1051 extends into the atmosphere above the height of measurements themselves.

1052 Furthermore, 15 cases when temperature profiles from the radiosonde observations  
1053 were the furthest away from the mean climatological average were selected, and ~~reproduced~~  
1054 the statistical comparison was reproduced over this subset of cases. These are the cases usually  
1055 the most difficult to retrieve and the most important to forecast; therefore, it is essential to  
1056 improve the retrievals in these situations. Even for this subset of selected cases ~~we find that~~  
1057 ~~MWRz2sigma449 produces better statistics, proving that the inclusion of active sensor~~  
1058 ~~observations in MWR passive observations would be beneficial for improving the accuracy of~~  
1059 ~~the retrieved temperature profiles also in the upper layer of the atmosphere where RASS~~  
1060 ~~measurements are not available (at least up to 5 km AGL). However, we note that this result~~  
1061 ~~may be dependent on the fact that our oblique measurements were taken at a 15-degree~~  
1062 ~~elevation angle, and that MWRs in locations with unobstructed views allowing for scans down~~  
1063 ~~to 5 degrees may provide similar improvements to the temperature profile accuracy in the~~  
1064 ~~lowest 0.1 or even 0.2 km AGL layers (Crewell and Löhnert, 2007); the inclusion of active sensor~~  
1065 observations in the PRs is found to be beneficial.

1066 Finally, ~~we also considered~~ the impact of the inclusion of RASS measurements on the  
1067 retrieved humidity profiles was considered, but ~~in this case~~ the inclusion of RASS observations  
1068 did not produce significantly better results, compared to the configurations that do not include  
1069 them. This was not a surprise as RASS measures virtual temperature, effectively adding very  
1070 little extra information to the water vapor ~~retrievals~~retrieval. In this case a better option would  
1071 be to consider adding other active remote sensors such as water vapor differential absorption  
1072 lidars (DIALs) to the PRs. Turner and Löhnert (~~2020~~2021) showed that including the partial  
1073 profile of water vapor observed by the DIAL substantially increases the information content in

Formatted: Line spacing: Double

1074 the combined water vapor retrievals. Consequently, to improve both temperature and humidity  
1075 retrievals a synergy between MWR, RASS, and DIAL systems would likely be necessary.

1076

## 1077 **Appendix A**

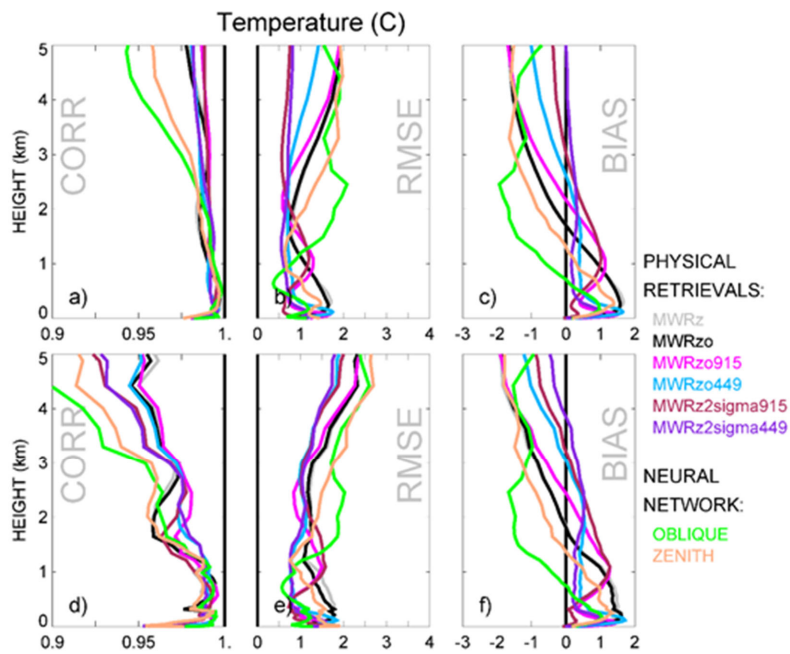
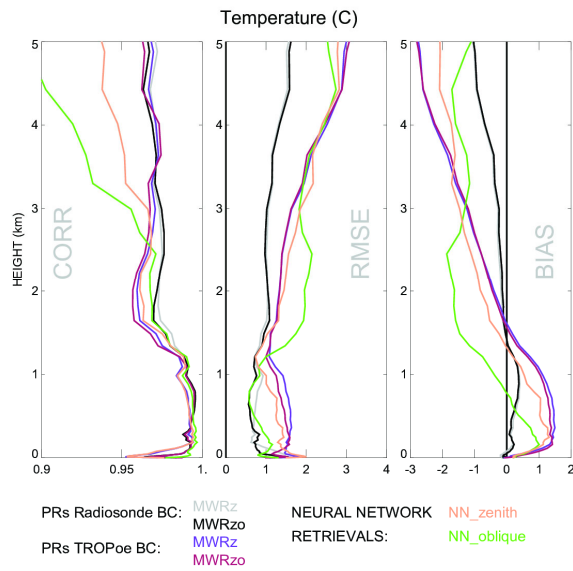
1078 The ~~XPIA neural network (NN)~~ retrievals developed by the vendor explicitly for XPIA use  
1079 a training dataset based on a 5-year climatology of profiles from radiosondes launched at the  
1080 Denver International Airport, 35 miles south-east from the XPIA site. NN-based MWR vertical  
1081 retrieval profiles were obtained using the zenith or an average of two oblique elevation scans,  
1082 15- and 165-degrees, (not including the zenith), all with 58 levels extending from the surface up  
1083 to 10 km, with nominal vertical levelsgrid depending on the height (every 50 m from the surface  
1084 to 500 m, every 100 m from 500 m to 2 km, and every 250 m from 2 to 10 km, AGL).

1085 Fig. 1A shows composite NN vertical profiles of temperature (separately for the zenith  
1086 and averaged obliques) calculated for radiosonde launch times, and the corresponding PR  
1087 profiles already introduced in Fig. 6. ~~As expected, the averaged oblique NN profile has lower  
1088 bias and RMSE compared to the zenith NN profile below 1km AGL, while the zenith NN profile  
1089 improved above this level.~~ 6a, b. For a proper comparison, only MWRz and MWRzo profiles are  
1090 used, without including RASS measurements. It has to be noted that since the "NN oblique"  
1091 retrieval provided by the manufacturer of the radiometer does not include the zenith, this  
1092 configuration cannot be considered exactly equivalent to the MWRzo PR.

Formatted: Indent: Left: 0", Hanging: 0.25"

Formatted: Line spacing: Double





1094  
1095  
1096  
1097  
1098  
1099  
1100  
1101  
1102  
1103  
1104  
1105  
1106  
1107  
1108  
1109  
1110  
1111  
1112  
1113  
1114  
1115

▲ *Fig. 1A. The same as Fig. 6 but with additional NN-Pearson correlation, RMSE, and mean bias for temperature profiles for MWRz in grey (and purple) and MWRzo in black (and maroon) when the radiosonde BC (and the TROPoe BC) method is applied. Included in this figure are the NN temperature profiles, from the zenith scan (in beige), and from the averaged oblique scans (in green).*

▲ ~~We note Another difference to point out is that in this comparison, while~~ the MWR Tb data have been bias-corrected before being used in the ~~Physical Retrieval~~PR configurations, as discussed in Section 3.2, ~~while~~ the NN retrievals use the uncorrected Tb, since it was non-trivial ~~for us~~ to reprocess those retrievals. ~~Zenith NN profiles~~Martinet et al. (2015) showed that when it is possible to bias-correct the MWR Tb before applying the NN retrieval technique, the NN retrievals are not impacted below 1 km AGL, but a clear improvement of NN retrievals in terms of RMSE and bias are observed between 1 and 3 km

**Formatted:** Font: *Italic*  
**Formatted:** Indent: First line: 0"  
**Formatted:** Space Before: 0 pt, After: 0 pt

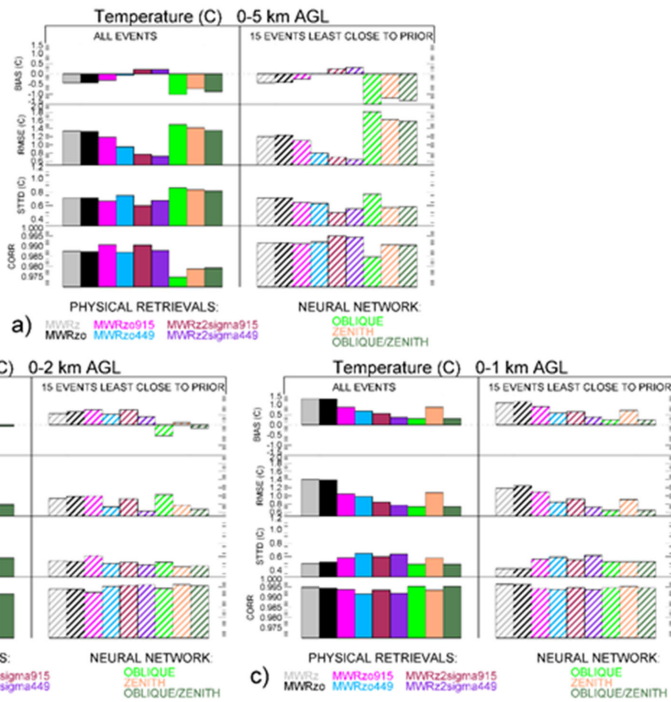
**Formatted:** Font: Not Italic  
**Formatted:** Indent: First line: 0.5", Space Before: 0 pt, After: 0 pt

1116 altitude. As is visible in Fig. 1A, this is the layer of the atmosphere where the NN profiles (beige  
1117 and green lines) have larger bias and RMSE ~~and smaller~~, compared to the PR profiles.

1118 When the radiosonde BC method is used, the MWRz and MWRzo PRs (gray and black  
1119 lines) present better statistics through the entire profiles shown in Fig. 1A, with larger values of  
1120 the correlation coefficient above 1 km AGL compared to all PR profiles. This is possibly due to  
1121 the Tb bias in the transparent channels of the V band frequencies, and smaller values of RMSE  
1122 and bias. The oblique only NN profiles (in green) show comparable statistics to the PRs  
1123 employing the radiosonde BC method up to 1 km AGL, with degraded performances above this  
1124 height. Above 1 km AGL, the zenith NN profiles (in beige) do better than the oblique NN in  
1125 terms of RMSE and bias. When the TROPoe BC method is used, the MWRz and MWRzo PRs  
1126 (purple and maroon lines) perform better than the NN profiles only in terms of RMSE and bias,  
1127 and above around 1.5 km AGL.

1128 —— To optimize the use of the two types of NN scan data, we combined the NN retrieved  
1129 profiles using only the averaged oblique scans up to 1 km AGL and the zenith scans above 1 km.  
1130 Fig. 2A is the same as Fig. 8, now including also the three NN profiles (averaged oblique only,  
1131 zenith only, and their combination) presenting the statistics in three different layers of  
1132 atmosphere: from the surface to 5 km AGL, from the surface to 2 km AGL, and from the surface  
1133 to 1 km AGL (a, b and c panels).

Formatted: Space Before: 0 pt, After: 0 pt



1134

1135 *Fig. 2A. The same as Fig. 8 but including NN profile statistics from averaged oblique scans in*  
 1136 *beige, from zenith—in green, and from their combination—in spruce. Panels a, b, and c show*  
 1137 *the temperature statistics from the surface up to 5, 2 and 1-km AGL respectively.*

1138 *—— Oblique only (and oblique and zenith combined) NN profiles show the best statistics in*  
 1139 *the layer closest to the surface, up to 1 km AGL, panel c, while in the deeper atmosphere layer*  
 1140 *up to 5 km all PR profiles have improved statistics compared to NNs, panel a. Panel b has mixed*  
 1141 *results: MWRz2sigma449 has the lowest RMSE, and the combined NN retrieved profiles show*  
 1142 *just slightly larger RMSE and almost the same standard deviation and correlation. It is*

1143 important to admit that while potential NN bias correction generally cannot change the oblique  
1144 statistics, it may improve the zenith profiles, especially above 1 km AGL, therefore improving  
1145 the combined NN profiles statistics.

1146 The better performance obtained by the MWRz and MWRzo PRs that use the  
1147 radiosonde BC approach demonstrate the importance of having an accurate and reliable  
1148 method for bias correcting the MWR.

1149 ▲  
1150 **Data availability**

1151 All data are publicly accessible at the DOE Atmosphere to Electrons Data Archive and  
1152 Portal, found at <https://a2e.energy.gov/projects/xpia> (Lundquist et al., 2016).

1153  
1154 **Author contribution**

1155 Irina Djalalova completed the primary analysis ~~with physical retrieval approach through~~  
1156 ~~MONORTM~~ using the XPIA data dataset. Daniel Gottas contributed to the post-processing of the  
1157 RASS data. Dave Turner modified the TROPoe algorithm to include the RASS data as input. All  
1158 authors contributed to the analysis of the results. Irina Djalalova prepared the manuscript with  
1159 contributions from all co-authors.

1160  
1161 **Acknowledgements**

1162 We thank all the people involved in XPIA for instrument deployment and maintenance,  
1163 data collection, and data quality control, and particularly the University of Colorado Boulder for

**Formatted:** Font: Not Italic

**Formatted:** Space Before: 0 pt, After: 0 pt, Border: Top: (No border), Bottom: (No border), Left: (No border), Right: (No border), Between : (No border)

**Formatted:** Indent: Left: 0", Hanging: 0.25"

**Formatted:** Indent: Left: 0", Hanging: 0.25"

**Formatted:** Line spacing: Double

1164 making the CU MWR data available. We are very grateful for the constructive comments and  
1165 suggestions provided by the two anonymous Referees and by the Editor, which we believe have  
1166 greatly improved the clarity of the manuscript. Funding for this study was provided by the  
1167 NOAA/ESRL Atmospheric Science for Renewable Energy (ASRE) program.

1168

1169

1170 Competing interests The authors declare no competing interests.

1171

## 1172 References

1173 Adachi, A., and H. Hashiguchi, H.: Application of parametric speakers to radio acoustic  
1174 sounding system. ATMOS MEAS TECH, **12**, 5699–5715, [https://doi.org/10.5194/amt-](https://doi.org/10.5194/amt-12-5699-2019)  
1175 [12-5699-2019](https://doi.org/10.5194/amt-12-5699-2019), 2019.

1176 Adler, B., J. M. Wilczak, J. M. L. Bianco, L. Djalalova, J. B. Duncan Jr., J. B. D. D. Turner, D. D.:  
1177 Observational case study of a persistent cold air pool and gap flow in the Columbia River  
1178 Basin, Under review to, J APPL METEOROL CLIM, **60**, 1071-1090,  
1179 <https://doi.org/10.1175/JAMC-D-21-0013.1>, 2021.

1180 Banta, R. M., and coauthors: Characterizing NWP model errors using Doppler lidar  
1181 measurements of recurrent regional diurnal flows: Marine-air intrusions into the  
1182 Columbia River Basin. MON WEATHER REV, **148**, 927-953,  
1183 <https://doi.org/10.1175/MWR-D-19-0188.1>, 2020.

1184 Bianco L., D. Cimini, D. F. S. Marzano, F. S., and R. Ware, R.: Combining microwave radiometer  
1185 and wind profiler radar measurements for high-resolution atmospheric humidity

Formatted: Indent: First line: 0.5"

Formatted: Indent: Left: 0", Hanging: 0.25"

Formatted: Default Paragraph Font, Font: Italic, Font color: Custom Color(RGB(17,85,204))

Formatted: Default Paragraph Font, Font: Italic

Field Code Changed

1186 profiling, *J ATMOS OCEAN TECH*, **22**, 949–965, <https://doi.org/10.1175/JTECH1771.1>,  
1187 2005.

**Formatted:** No underline

1188 Bianco, L., [K. Friedrich](#), [K. J. M. Wilczak](#), [J. M. D. Hazen](#), [D. Wolfe](#), [D. R. Delgado](#), [R. S. Oncley](#),  
1189 [S.](#), and [J. K. Lundquist](#), [J. K.](#): Assessing the accuracy of microwave radiometers and radio  
1190 acoustic sounding systems for wind energy applications. *ATMOS MEAS TECH*, **10**, 1707-  
1191 1721, <https://doi.org/10.5194/amt-10-1707-2017>, 2017.

**Formatted:** Font: Not Bold

**Formatted:** No underline

1192 Cadeddu, M. P., [J. C. Liljegren](#), [J. C.](#), and [D. D. Turner](#), [D. D.](#): The Atmospheric radiation  
1193 measurement (ARM) program network of microwave radiometers: instrumentation,  
1194 data, and retrievals, *ATMOS MEAS TECH*, **6**, 2359–2372, [https://doi.org/10.5194/amt-6-](https://doi.org/10.5194/amt-6-2359-2013)  
1195 [2359-2013](https://doi.org/10.5194/amt-6-2359-2013), 2013.

**Formatted:** No underline

1196 Cimini, D., [T. J. Hewison](#), [T. J. L. Martin](#), [L. J. Guldner](#), [J. C. Gaffard](#), [C. F. S. Marzano](#), [F. S.](#):  
1197 Temperature and humidity profile retrievals from ground-based microwave radiometers  
1198 during TUC,  
1199 *METEOROL Z*, Vol. 15, No. 5, 45-56, [DOI: 10.1127/09411-D-2948/2006/0099](https://doi.org/10.1127/09411-D-2948/2006/0099), 2006.

**Formatted:** Font color: Custom Color(17,85,204)

**Formatted:** Font color: Custom Color(17,85,204)

**Formatted:** No underline

1200 Cimini, D., [E. Campos](#), [E. R. Ware](#), [R. S. Albers](#), [S. G. Giuliani](#), [G. J. Oreamuno](#), [J. P. Joe](#), [P. S. E.](#)  
1201 Koch, S., [E. Cober](#), [S.](#) and [E. Westwater](#), [E.](#): Thermodynamic Atmospheric Profiling  
1202 during the 2010 Winter Olympics Using Ground-based Microwave Radiometry, *IEEE T*  
1203 *GEOSCI REMOTE*, **49**, 12, <https://doi.org/10.1109/TGRS.2011.2154337>, 2011.

**Formatted:** No underline

1204 Cimini, D., Rosenkranz, P. W., Tretyakov, M. Y., Koshelev, M. A., and Romano, F.: Uncertainty of  
1205 atmospheric microwave absorption model: impact on ground-based radiometer  
1206 simulations and retrievals, *ATMOS CHEM PHYS*, **18**, 15231–15259,  
1207 <https://acp.copernicus.org/articles/18/15231/2018/>, 2018.

**Formatted:** Font: Not Bold

**Formatted:** Font: Not Italic

**Formatted:** Font color: Custom Color(17,85,204)

**Formatted:** Font color: Custom Color(17,85,204)

**Formatted:** No underline

1208 Cimini, D., M. Haeffelin, M. S. Kotthaus, S. U. Löhnert, U. P. Martinet, P. E. O'Connor, E. C.  
1209 Walden, C. M. Collaud Coen, M., and J. Preissler, J.: Towards the profiling of the  
1210 atmospheric boundary layer at European scale—introducing the COST Action PROBE,  
1211 **Bulletin of Atmospheric Science and Technology**, **1**, 23–42,  
1212 <https://doi.org/10.1007/s42865-020-00003-8>, 2020.

1213 Clough, S.A., M. W. Shephard, M. W. E. J. Mlawer, E. J. S. Delamere, J. S. M. Iacono, M. K. E.  
1214 Cady-Pereira, K. E. S. Boukabara, S., and P. D. Brown, P. D.: Atmospheric radiative  
1215 transfer modeling: A summary of the AER codes, **J QUANT SPECTROSC RA**, vol 91, no. 2,  
1216 pp 233-244, <https://doi.org/10.1016/j.jqsrt.2004.05.058>, 2005.

1217 Crewell, S., U. Löhnert, U.: Accuracy of Boundary Layer Temperature Profiles Retrieved With  
1218 Multifrequency Multiangle Microwave Radiometry, **IEEE T GEOSCI REMOTE**, VOL. 45,  
1219 NO. 7, JULY 2007, [DOI: 10.1109/TGRS.2006.888434](https://doi.org/10.1109/TGRS.2006.888434) DOI: 10.1109/TGRS.2006.888434,  
1220 2007.

1221 Engelbart, D., W. Monna, W. J. Nash, J.: Integrated Ground-Based Remote-Sensing Stations for  
1222 Atmospheric Profiling, **COST Action 720 Final Report**, EUR 24172,  
1223 <https://doi.org/10.2831/10752>, 2009.

1224 Görsdorf, U., and V. Lehmann, V.: Enhanced Accuracy of RASS-Measured Temperatures Due to  
1225 an Improved Range Correction, **J ATMOS OCEAN TECH**, **17 (4)**, 406–416,  
1226 [https://doi.org/10.1175/1520-0426\(2000\)017<0406:EAORMT>2.0.CO;2](https://doi.org/10.1175/1520-0426(2000)017<0406:EAORMT>2.0.CO;2), 2000.

1227 Han, Y., and E. R. Westwater, E. R.: Remote sensing of tropospheric water vapor and cloud  
1228 liquid water by integrated ground-based sensors, **J ATMOS OCEAN TECH**, **12**, 1050-

Formatted: No underline

Formatted: No underline

Formatted: No underline

Formatted: No underline



1229 1059, DOI: [https://doi.org/10.1175/1520-0426\(1995\)012<1050:RSOTWV>2.0.CO;2](https://doi.org/10.1175/1520-0426(1995)012<1050:RSOTWV>2.0.CO;2),  
1230 [https://doi.org/10.1175/1520-0426\(1995\)012<1050:RSOTWV>2.0.CO;2](https://doi.org/10.1175/1520-0426(1995)012<1050:RSOTWV>2.0.CO;2), 1995.  
1231 Hewison, T.: 1D-VAR Retrieval of Temperature and Humidity Profiles From a Ground-Based  
1232 Microwave Radiometer, **IEEE T GEOSCI REMOTE**, **45(7)**, 2163–2168,  
1233 <https://doi.org/10.1109/TGRS.2007.898091>, 2007.  
1234 Horst, T. W., [S. R. Semmer](#), [S. R.](#), and [I. Bogoev](#), [I.](#): Evaluation of Mechanically-Aspirated  
1235 Temperature/Relative Humidity Radiation Shields, 18th Symposium on Meteorological  
1236 Observation and Instrumentation, AMS Annual Meeting, New Orleans, LA, 10-15  
1237 January 2016, <https://ams.confex.com/ams/96Annual/webprogram/Paper286839.html>,  
1238 2016.  
1239 Kaimal, J. C., and [J. E. Gaynor](#), [J. E.](#): The Boulder Atmospheric Observatory, **J CLIM APPL**  
1240 **METEOROL**, **22**, 863–880, [https://doi.org/10.1175/1520-](https://doi.org/10.1175/1520-0450(1983)022<0863:TBAO>2.0.CO;2)  
1241 [0450\(1983\)022<0863:TBAO>2.0.CO;2](https://doi.org/10.1175/1520-0450(1983)022<0863:TBAO>2.0.CO;2), 1983.  
1242 Küchler, N., [D. D. Turner](#), [D. D. U. Löhnert](#), [U.](#), and [S. Crewell](#), [S.](#): Calibrating ground-based  
1243 microwave radiometers: Uncertainty and drifts, **RADIO SCI**, **51**, 311–  
1244 327, [doi:10.1002/2015RS005826](https://doi.org/10.1002/2015RS005826), [doi:10.1002/2015RS005826](https://doi.org/10.1002/2015RS005826), 2016.  
1245 Löhnert U. and [O. Maier](#), [O.](#): Operational profiling of temperature using ground-based  
1246 microwave radiometry at Payerne: prospects and challenges, **ATMOS MEAS TECH**, **5**,  
1247 1121–1134, <https://doi.org/10.5194/amt-5-1121-2012>, 2012.  
1248 Lundquist, J. K., [J. M. Wilczak](#), [J. M. R. Ashton](#), [R. L. Bianco](#), [L. W. A. Brewer](#), [W. A. Choukulkar](#),  
1249 [A. Clifton](#), [A. M. Debnath](#), [M. R. Delgado](#), [R. K. Friedrich](#), [K. S. Gunter](#), [S. A. Hamidi](#),  
1250 [A. G. V. Iungo](#), [G. V. A. Kaushik](#), [A. B. Kosović](#), [B. P. Langan](#), [P. A. Lass](#), [A. E. Lavin](#), [E. Lee](#),

Formatted: No underline

Formatted: No underline

Formatted: No underline

Formatted: No underline

Formatted: No underline

1251 J. C.-Y., Lee, K. L. McCaffrey, R. K., Newsom, R. K., D. C. Noone, D. C., S. P. Oncley, S.-P.,  
1252 I. Quelet, S. P.-T., Sandberg, S.-P., J. L. Schroeder, W. J., Shaw, W.-J., L. Sparling, L., C. St.  
1253 Martin, CA. St., Pe, A.-St., E. Strobach, E., K. Tay, K., B. J. Vanderwende, B.-J., A.  
1254 Weickmann, A., D. Wolfe, D., and R. Worsnop, R.: Assessing state-of-the-art capabilities  
1255 for probing the atmospheric boundary layer: the XPIA field campaign. **B AM METEOROL**  
1256 **SOC, 98**, 289–314, <https://doi.org/10.1175/BAMS-D-15-00151.1>, 2017.

1257 Maahn, M., D. D. Turner, D.-D., U. Löhnert, U., D. J. Posselt, D.-J., K. Ebell, K., G. G. Mace, G.-G.,  
1258 and J. M. Comstock, J.-M.: Optimal estimation retrievals and their uncertainties: What  
1259 every atmospheric scientist should know. **B AM METEOROL SOC, 101**, E1512-E1523,  
1260 <https://doi.org/10.1175/BAMS-D-19-0027.1>, 2020.

1261 Maddy, E. S. and C. D. Barnett, C.-D.: Vertical Resolution Estimates in Version 5 of AIRS  
1262 Operational Retrievals. **IEEE T GEOSCI REMOTE, VOL. 46**, NO. 8, AUGUST 2008,  
1263 <https://doi.org/10.1109/TGRS.2008.917498>, 2008.

1264 Martinet, P., A. Dabas, J.-M. Donier, T. Douffet, O. Garrouste, and R. Guillot: 1D-Var  
1265 temperature retrievals from microwave radiometer and convective scale model, TELLUS  
1266 A, 67:1, https://doi.org/10.3402/tellusa.v67.27925, 2015.

1267 Martinet, P., D. Cimini, D.-F. Burnet, F.-B. Ménérier, B.-Y. Michel, Y., and V. Unger, V.:  
1268 Improvement of numerical weather prediction model analysis during fog conditions  
1269 through the assimilation of ground-based microwave radiometer observations: a 1D-Var  
1270 study, **ATMOS MEAS TECH, 13**, 6593–6611, <https://doi.org/10.5194/amt-13-6593-2020>,  
1271 2020.

Formatted: No underline

Field Code Changed

Formatted: Default Paragraph Font, Font: Italic, Font color: Custom Color(RGB(17,85,204))

Formatted: No underline

Formatted: No underline

1272 May, P. T. and J. M. Wilczak, J. M.: Diurnal and Seasonal Variations of Boundary-Layer Structure  
1273 Observed with a Radar Wind Profiler and RASS. **MON WEATHER REV**, **121**, 673–682,  
1274 [https://doi.org/10.1175/1520-0493\(1993\)121<0673:DASVOB>2.0.CO;2](https://doi.org/10.1175/1520-0493(1993)121<0673:DASVOB>2.0.CO;2), 1993.

1275 Masiello, G., C. Serio, C., and P. Antonelli, P.: Inversion for atmospheric thermodynamical  
1276 parameters of IASI data in the principal components space. **Q J ROY METEOR SOC**, **138**,  
1277 103–117, <https://doi.org/10.1002/qj.909>, 2012.

1278 Merrelli, A. M., and D. D. Turner, D. D.: Comparing information content of upwelling far  
1279 infrared and midinfrared radiance spectra for clear atmosphere profiling. **J ATMOS**  
1280 **OCEAN TECH**, **29**, 510–526, <https://doi.org/10.1175/JTECH-D-11-00113.1>, 2012.

1281 Neiman, P. J., D. J. Gottas, D. J., and A. B. White, A. B.: A Two-Cool-Season Wind Profiler–Based  
1282 Analysis of Westward-Directed Gap Flow through the Columbia River Gorge. **MON**  
1283 **WEATHER REV**, **147**, 4653–4680, <https://doi.org/10.1175/MWR-D-19-0026.1>, 2019.

1284 North, E. M., A. M. Peterson, A. M., and H. D. Parry, H. D.: RASS, a remote sensing system for  
1285 measuring low-level temperature profiles. **B AM METEOROL SOC**, **54**, 912–919, 1973.

1286 Payne, V. H., J. S. Delamere, J. S., K. E. Cady-Pereira, K. E., R. R. Gamache, R. R., J.-L. Moncet, E. J.  
1287 Mlawer, E. J., and E. J. S. A. Clough, E. J.: Air-broadened half-widths of the 22- and  
1288 183-GHz water-vapor lines. **IEEE T GEOSCI REMOTE**, **46**, 3601–3617,  
1289 <https://doi.org/10.1109/TGRS.2008.2002435><https://doi.org/10.1109/TGRS.2008.2002435>  
1290 <https://doi.org/10.1109/TGRS.2008.2002435>  
1291 <https://doi.org/10.1109/TGRS.2008.2002435>, 2008.

1291 Payne, V. H., E. J. Mlawer, E. J., K. E. Cady-Pereira, K. E., and J.-L. Moncet, J.-L.: Water vapor  
1292 continuum absorption in the microwave. **IEEE T GEOSCI REMOTE**, **49**, 2194–2208,

**Formatted:** No underline

**Formatted:** No underline

**Formatted:** No underline

**Formatted:** No underline

**Formatted:** Default Paragraph Font, Font: Italic

**Formatted:** Space After: 0 pt

1293 <https://doi.org/10.1109/TGRS.2010.2091416><https://doi.org/10.1109/TGRS.2010.20914>  
1294 [16](https://doi.org/10.1109/TGRS.2010.20914), 2011.

**Formatted:** Default Paragraph Font, Font: Italic

1295 Rodgers, C. D.: Inverse Methods for Atmospheric Sounding: Theory and Practice. Series on  
1296 Atmospheric, Oceanic and Planetary Physics, Vol. 2, World Scientific, 238 pp, 2000.

1297 Rosenkranz, P. W.: Water vapour microwave continuum absorption: A comparison of  
1298 measurements and models. **RADIO SCI**, **33**, 919–928,

1299 <https://doi.org/10.1029/98RS01182><https://doi.org/10.1029/98RS01182>, 1998.

**Formatted:** Default Paragraph Font, Font: Italic

1300 Shaw, W., and Coauthors: The Second Wind Forecast Improvement Project (WFIP 2): General  
1301 Overview. **B AM METEOROL SOC**, **100(9)**, 1687–1699, [https://doi.org/10.1175/BAMS-](https://doi.org/10.1175/BAMS-D-18-0036.1)  
1302 [D-18-0036.1](https://doi.org/10.1175/BAMS-D-18-0036.1), 2019.

**Formatted:** No underline

1303 Solheim, F., [J. R. Godwin](#), [J. R.](#), and [R. Ware](#). Passive ground-based remote sensing of  
1304 atmospheric temperature, water vapor, and cloud liquid profiles by a frequency  
1305 synthesized microwave radiometer. **METEOROL Z**, **7**, 370–376, 1998a.

**Formatted:** Font color: Black

1306 Solheim F., [J. R. Godwin](#), [J. R.](#), Westwater, [E. R.](#), [Y. Han](#), [Y. S. J. Keihm](#), [S. J. K. Marsh](#), [K. R.](#)  
1307 [Ware](#). Radiometric profiling of temperature, water vapor and cloud liquid water  
1308 using various inversion methods. **RADIO SCI**, **33**, 393–404,  
1309 <https://doi.org/10.1029/97RS03656>, 1998b.

**Formatted:** No underline, Font color: Black

1310 Stankov, B. B., [E. R. Westwater](#), [E. R.](#), and [E. E. Gossard](#). Use of wind profiler estimates of  
1311 significant moisture gradients to improve humidity profile retrieval. **J ATMOS OCEAN**  
1312 **TECH**, **13**, 1285-1290, DOI: [https://doi.org/10.1175/1520-](https://doi.org/10.1175/1520-042615200426(1996)013<1285:UOWPEO>2.0.CO;2)

**Field Code Changed**

1313 [042615200426\(1996\)013<1285:UOWPEO>2.0.CO;2](https://doi.org/10.1175/1520-042615200426(1996)013<1285:UOWPEO>2.0.CO;2), 1996.

**Formatted:** Default Paragraph Font, Font: Italic

1314 Strauch, R. G., D. A. Merritt, D. A. K. P. Moran, K. P., B. Earnshaw, K. B., and D. V. De Kamp, D.  
1315 V.: The Colorado wind-profiling network. **J ATMOS OCEAN TECH**, **1**, 37–49,  
1316 [https://doi.org/10.1175/1520-0426\(1984\)001<0037:tcwpm>2.0.co;2](https://doi.org/10.1175/1520-0426(1984)001<0037:tcwpm>2.0.co;2), 1983.

Formatted: No underline

1317 Turner, D. D., and U. Löhnert, U.: Information content and uncertainties in thermodynamic  
1318 profiles and liquid cloud properties retrieved from the ground-based Atmospheric  
1319 Emitted Radiance Interferometer (AERI). **J APPL METEOROL CLIM**, **53**, 752–771,  
1320 <https://doi.org/10.1175/JAMC-D-13-0126.1>, 2014.

Formatted: No underline

1321 Turner, D. D., and W. G. Blumberg, W. G.: Improvements to the AERIoe thermodynamic profile  
1322 retrieval algorithm. **IEEE J-STARS**, **12(5)**, 1339–1354,  
1323 <https://doi.org/10.1109/JSTARS.2018.2874968>, 2019.

Formatted: No underline

1324 Turner, D. D., and U. Löhnert, U.: Ground-based Temperature and Humidity Profiling:  
1325 Combining Active and Passive Remote Sensors. *In revision to*, **ATMOS MEAS TECH**,  
1326 <https://doi.org/10.5194/amt-2020-35214>, 3033–3048, [https://doi.org/10.5194/amt-](https://doi.org/10.5194/amt-2020-352)  
1327 [2020-352](https://doi.org/10.5194/amt-2020-352), [20202021](https://doi.org/10.5194/amt-2020-352).

Formatted: No underline

1328 Ware R., Carpenter R., Güldner, J., Liljegren, J., Nehr Korn, T., Solheim F., and Vandenberghe  
1329 F.; Ware R., Solheim F., Carpenter R., and Coauthors: A multi-channel radiometric  
1330 profiler of temperature, humidity and cloud liquid. **RADIO SCI**, **38**, No. 4, 8079,  
1331 <https://doi.org/10.1029/2002RS002856>, 2003.

Formatted: No underline

Formatted: Font color: Blue

1332 Weber, B. L., D. B. Wuertz, D. B. C. Welsh, D. C., and R. Mcpeak, R.: Quality controls for profiler  
1333 measurements of winds and RASS temperatures. **J ATMOS OCEAN TECH**, **10**, 452–464,  
1334 [https://doi.org/10.1175/1520-0426\(1993\)010<0452:qcfpmo>2.0.co;2](https://doi.org/10.1175/1520-0426(1993)010<0452:qcfpmo>2.0.co;2), 1993.

Formatted: No underline

1335 Wilczak, J. M., and Coauthors: The Second Wind Forecast Improvement Project (WFIP2):

1336 Observational Field Campaign. **B AM METEOROL SOC**, **100(9)**, 1701–1723,

1337 <https://doi.org/10.1175/BAMS-D-18-0035.1>, 2019.

**Formatted:** No underline

1338 Wolfe, D. E. and ~~R. J. Lataitis, R. J.~~, Boulder Atmospheric Observatory: 1977–2016: The end of

1339 an era and lessons learned. **B AM METEOROL SOC**, **99**, 1345–1358,

1340 <https://doi.org/10.1175/BAMS-D-17-0054.1>, 2018.

**Formatted:** No underline